# Machine Learning Gravitational Waveforms for Binary Neutron Star mergers

Jacopo Tissino

2021-09-08

**Abstract**

The analysis of interferometric data corresponding to the gravitational waves emitted in a binary neutron star merger requires the generation of numerous theoretical waveforms. In this thesis, I develop a machine learning algorithm trained on frequency-domain waveforms generated through the effective one-body technique, which is able to reconstruct them accurately and with a speed improvement.

## Introduction

[INTRODUCTION IS STILL PROVISIONAL]

The detection of a gravitational wave (GW) signal from the binary neutron star (BNS) merger GW170817 [Abb+17] opened a new avenue for the direct study of neutron star properties, such as their masses, spins and equations of state.

The study of an observed signal is done through Bayesian parameter estimation algorithms, which require the comparison of the experimental signal with several million [Lac+17] simulated waveforms or more (see section 1.3). Speed in the generation of simulated waveforms is, therefore, crucial.

There are three main strategies for the generation of these waveforms. In order of decreasing evaluation time, as well as (typically) decreasing accuracy, they are:

1. full numerical relativity (NR) simulations: these are our most accurate possible avenue for the study of BNS mergers, but they are so computationally expensive that it is reasonable to simulate at most a few tens of initial condition setups — these are then used to validate the other methods (see section 1.4.2);

2. effective one-body (EOB) simulations: these consist in constructing an effective Hamiltonian for a test particle as a proxy for the two-body system and simulating its evolution — they can be calibrated by comparison to NR simulations (see section 1.4.3);

3. post-Newtonian (PN) waveforms: here we expand the equations of motion of the system in powers of $1/c^2$ and analytically calculate the evolution of the amplitude and phase of the waveform (see section 1.4.1).

The EOB and PN formalisms can be complemented with a tidal term, which is relevant for BNS mergers: neutron stars (as opposed to black holes) can be deformed by each other's gravitational field in a way which depends on the specifics of their equation of state.

The evaluation times for EOB waveforms are dependent on the duration of the waveforms: GW170817 lasted for about two minutes, and the generation of waveforms of this length takes on the order of 100ms with state-of-the-art systems, but as the noise in ground-based interferometers decreases we expect to be able to see a longer and longer section of the waveform, which might bring the evaluation times back above 1s.

Also, the waveforms ought to be generated in the frequency domain, since that form is the one which is used in data analysis; EOB models, on the other hand, natively generate waveforms in the time domain.

The work in this thesis is an attempt to make progress in this direction, by developing a machine learning system trained on the (Fourier transforms of the) EOB waveforms. This builds on the work of Schmidt et al. [Sch+20], who developed a similar system to generate Binary Black Hole merger waveforms in the time domain.

The algorithm's basic components are as follows:

- a training dataset is generated by considering uniformly distributed tuples of BNS parameters in the allowed ranges and calculating the corresponding waveforms with the EOB model `TEOBResumS` [Nag+18];

- each time-domain waveform is Fourier-transformed and decomposed into phase and amplitude;

- each EOB waveform is compared to a PN one with the same parameters, and a dataset is constructed from the residuals of the EOB waveform from the PN one;

- the dimensionality of the training dataset is reduced through principal component analysis (PCA);

- a feed-forward neural network is trained to reconstruct the map between the BNS system parameters and the PCA components of the waveforms.

The resulting model must be evaluated in terms of both speed and accuracy. Regarding the former, proper benchmarking will begin at a later stage, but the results obtained by Schmidt et al. [Sch+20] indicate the possibility of obtaining a speedup of one to two orders of magnitude compared to EOB algorithms.

Regarding the latter, preliminary results indicate the possibility of the model reconstructing EOB waveforms with three parameters (the mass ratio $q$ and the two tidal deformabilities $\Lambda_1$ and $\Lambda_2$) with a maximal unfaithfulness of the order of $\mathcal{F} \simeq 10^{-3}$. This is comparable to typical values of the unfaithfulness of EOB waveforms compared to NR ones ($\mathcal{F} \simeq 2.5 \times 10^{-3}$ [Nag+18]).

This indicates that it is possible for this system to become a part of a gravitational wave data analysis pipeline, enabling a significant speedup at the cost a small, tolerable loss in accuracy.

Possible applications of the software developed in this work include modelled signal searches and parameter estimation for both current interferometers (such as LIGO and Virgo) and for future ones, such as Einstein Telescope.

# 1 Gravitational wave theory

## 1.1 Linearized gravity

The simplest way to discuss gravitational radiation is to consider linearized gravity on a flat Minkowskian background.

This means that we assume that our spacetime admits a reference frame for which the metric is in the form

$$g_{\mu\nu} = \eta_{\mu\nu} + h_{\mu\nu}, \tag{1.1}$$

where the value of the components $h_{\mu\nu}$ is small enough that we can work to first order in them. Any equation in this section includes an implicit "$+\mathcal{O}\left(h^2\right)$". We work in this *global inertial frame*.

In order to study the evolution of the perturbation $h_{\mu\nu}$ we need to solve the Einstein Field Equations for it to linear order. In a vacuum, they can be written as

$$G_{\mu\nu} = R_{\mu\nu} - \frac{1}{2}\eta_{\mu\nu}R = 0 \tag{1.2}$$

$$R_{\mu\nu} = g^{\alpha\beta}R_{\alpha\mu\beta\nu} \tag{1.3}$$

$$R = g^{\mu\nu}R_{\mu\nu}, \tag{1.4}$$

where $R_{\alpha\mu\beta\nu} \sim \partial\Gamma + \Gamma\Gamma$ is the Riemann tensor, which is written in terms of derivatives and squares of Christoffel symbols $\Gamma$:

$$\Gamma^\rho_{\mu\nu} = \frac{1}{2}g^{\rho\lambda}\left(\partial_\mu g_{\nu\lambda} + \partial_\nu g_{\lambda\mu} - \partial_\lambda g_{\mu\nu}\right) \tag{1.5}$$

$$= \frac{1}{2}\eta^{\rho\lambda}\left(\partial_\mu h_{\nu\lambda} + \partial_\nu h_{\lambda\mu} - \partial_\lambda h_{\mu\nu}\right). \tag{1.6}$$

We use the fact that $\partial\eta = 0$, and keep only linear order terms.

Since the Christoffel symbols are of first order in the perturbation, the term $\Gamma\Gamma$ in the Riemann tensor is of second order and can be neglected. Therefore, the relevant components are

$$R_{\mu\nu\rho\sigma} = 2\eta_{\mu\lambda}\Gamma^\lambda_{\nu[\sigma,\rho]} = h_{\mu[\sigma,\rho]\nu} - h_{\nu[\sigma,\rho]\mu}, \tag{1.7}$$

which gives us the following expression for the Ricci tensor:

$$R_{\mu\nu} = \frac{1}{2}\left(h^\sigma{}_{\mu,\sigma\nu} + h^\sigma{}_{\nu,\sigma\mu} - h_{,\mu\nu} - \Box h_{\mu\nu}\right), \tag{1.8}$$

where $h = \eta^{\mu\nu}h_{\mu\nu}$ is the trace of the perturbation (computed with respect to the flat metric), while $\Box = \eta^{\mu\nu}\partial_\mu\partial_\nu$ is the flat space d'Alambertian.

3

This, in turn, allows us to write out the Einstein tensor:

$$G_{\mu\nu} = \frac{1}{2}\left(h^{\sigma}{}_{\mu,\sigma\nu} + h^{\sigma}{}_{\nu,\sigma\mu} - h_{,\mu\nu} - \Box h_{\mu\nu} - \eta_{\mu\nu}h^{\rho\lambda}{}_{,\rho\lambda} + \eta_{\mu\nu}\Box h\right). \tag{1.9}$$

This can be greatly simplified with two steps: first, we change variable from the perturbation $h_{\mu\nu}$ to the *trace-reversed* perturbation $\bar{h}_{\mu\nu} = h_{\mu\nu} - \eta_{\mu\nu}h/2$ — the name comes from the fact that $\eta^{\mu\nu}\bar{h}_{\mu\nu} = -h$.

This substitution allows us to write the Einstein tensor as

$$G_{\mu\nu} = -\frac{1}{2}\Box\bar{h}_{\mu\nu} + \bar{h}_{\alpha(\mu,\nu)}{}^{\alpha} - \frac{1}{2}\eta_{\mu\nu}\bar{h}_{\alpha\beta}{}^{,\alpha\beta}. \tag{1.10}$$

We will shortly show that it is possible, as a *gauge choice*, to set the divergence of the trace-reversed perturbation to zero: $\partial^{\mu}\bar{h}_{\mu\nu} = 0$ (see section 1.1.2). The gauge imposed by this choice is called the *Hilbert Gauge*,[1] which in terms of the regular perturbation reads

$$\partial^{\mu}h_{\mu\nu} - \frac{1}{2}\partial_{\nu}h = 0. \tag{1.11}$$

With this choice the Einstein tensor becomes simply

$$G_{\mu\nu} = -\frac{1}{2}\Box\bar{h}_{\mu\nu}, \tag{1.12}$$

so the general form of the Einstein equations to linear order will be

$$\Box\bar{h}_{\mu\nu} = -16\pi G\, T_{\mu\nu}\Big|_{\text{linear}}, \tag{1.13}$$

where the stress-energy tensor is computed up to first order in the metric perturbation.

### 1.1.1 Transformations of the perturbation

The theory of General Relativity is constructed to be invariant under smooth changes of coordinates: under a map in the form $x \to x' = x'(x)$ (where $x'(x)$ is a diffeomorphism[2]).

Under such a coordinate transformation the metric transforms like any $(0,2)$ tensor:

$$g'_{\alpha\beta}(x') = \frac{\partial x^{\mu}}{\partial x'^{\alpha}}\frac{\partial x^{\nu}}{\partial x'^{\beta}}g_{\mu\nu}(x). \tag{1.14}$$

A general transformation of this kind may break the condition that $g = \eta + h$ where $h$ is small, so in order to preserve our framework we restrict ourselves to a small class of transformations.

---

[1] Despite the name, this choice was first suggested by De Sitter to Einstein [Ken07], who had been previously trying to impose the gauge $|g| = 1$ [Ein16, page 688].

[2] In the physics parlance this property is known as "diffeomorphism invariance", while a mathematician would call the kinds of transformations considered "isometries", since we ask that they preserve the metric structure of the manifold.

One possibility is to consider infinitesimal transformations in the form

$$x^\mu \to x'^\mu = x^\mu + \xi^\mu(x), \tag{1.15}$$

where $\xi^\mu$ is a vector field such that $\left|\partial_\mu \xi_\nu\right|$ is small — specifically, the condition to impose is that the first order in $\partial_\mu \xi_\nu$ should match the first order in $h_{\mu\nu}$.

This condition is all we need in order to write the transformation law for the perturbation: the full equation reads

$$\eta'_{\mu\nu} + h'_{\mu\nu} \approx \left(\delta^\alpha_\mu - \partial^\alpha \xi_\mu\right)\left(\delta^\beta_\nu - \partial^\beta \xi_\nu\right)\left(\eta_{\alpha\beta} + h_{\mu\nu}\right), \tag{1.16}$$

Used $1/(1+x) = 1 - x + \mathcal{O}(x^2)$.

so the zeroth order contribution is $\eta'_{\mu\nu} = \eta_{\mu\nu}$, while the first order one is

$$\boxed{h'_{\mu\nu} = h_{\mu\nu} - 2\partial_{(\mu}\xi_{\nu)},} \tag{1.17}$$

which is our transformation law for the metric perturbation.

We will also need a transformation law for the trace-reversed perturbation $\overline{h}_{\mu\nu}$: the trace transforms as $h' \to h - 2\partial_\mu \xi^\mu$, therefore the required law is

$$\overline{h}'_{\mu\nu} = \overline{h}_{\mu\nu} - 2\partial_{(\mu}\xi_{\nu)} + \eta_{\mu\nu}\partial_\alpha \xi^\alpha. \tag{1.18}$$

A second class of transformations which sometimes preserve the structure $g = \eta + h$ is a subset of Lorentz boosts and rotations: substituting $\partial x^\mu / \partial x'^\nu = \Lambda_\nu{}^\mu$ into the transformation law (1.14) we find that the flat metric is unchanged, while

$$h'_{\mu\nu}(x') = \Lambda_\mu{}^\alpha \Lambda_\nu{}^\beta h_{\alpha\beta}, \tag{1.19}$$

which may remain in the class of small metric perturbations: this is not guaranteed, but it is true for a certain subset of boosts and for all rotations [Mag07].

Finally, the perturbation is invariant under shifts in the form $x'^\mu = x^\mu + a^\mu$.

### 1.1.2 Gauge fixing

Now that we know how the perturbation $h_{\mu\nu}$ transforms under an infinitesimal transformation, we can use this to impose the condition we want — specifically, the Hilbert gauge (1.11).

The way to show that this is possible is to write out the way $\partial^\mu \overline{h}_{\mu\nu}$ transforms for an arbitrary choice of $\xi$, and to see that with an appropriate choice of $\xi$ we can always map it to zero. The transformation reads

$$\partial^\mu \overline{h}'_{\mu\nu} = \partial^\mu\left(h_{\mu\nu} - 2\partial_{(\mu}\xi_{\nu)}\right) - \frac{1}{2}\partial_\nu\left(\eta^{\alpha\beta}\left(h_{\alpha\beta} - 2\partial_{(\alpha}\xi_{\beta)}\right)\right) \tag{1.20}$$

$$= \partial^\mu \overline{h}_{\mu\nu} - \Box\xi_\nu - \partial_\nu\left(\partial^\mu \xi_\mu\right) + \partial_\nu\left(\partial^\mu \xi_\mu\right) \tag{1.21}$$

$$= \partial^\mu \overline{h}_{\mu\nu} - \Box\xi_\nu. \tag{1.22}$$

Therefore, from any starting gauge we must only find a $\xi_\nu$ such that $\partial^\mu \bar{h}_{\mu\nu} = \Box \xi_\nu$, and we will be in the correct gauge. This can always be done, since the D'Alambert equation $\Box f = g$ can always be solved for $f$ — if we needed to compute $\xi_\nu$ explicitly (which we typically do not) we could use the Green's function $G(z)$ for the operator, defined by $\Box G(z) = \delta^{(4)}(z)$.

While the equation is solvable, the solution is not unique: if we were to define an "inverse" of the D'Alambertian it would not be a function but a one-to-many relation. Specifically, while keeping fixed the value of $\Box \xi_\nu$ we can add any function $\zeta_\nu$ to $\xi_\nu$ as long as $\Box \zeta_\nu = 0$. A trivial example is $\zeta_\nu = \text{const}$, but other wave-like choices are of more interest.

These still induce a transformation on $h_{\mu\nu}$ according to the usual law (1.17), and they can be used to further specify the form of the gravitational radiation.

In terms of **degrees of freedom**, the full perturbation $h_{\mu\nu}$ starts with 10 as any symmetric 4D, rank-2 tensor; the four Hilbert gauge conditions (1.11) reduce them to 6, while the four residual gauge conditions will allow us, under some specific assumptions, to reduce them to 2.

Let us fix the residual gauge in the specific context of a plane wave solution to the wave equation $\Box \bar{h}_{\mu\nu} = 0$.

### 1.1.3   Plane gravitational waves

A general solution to the wave equation may be written as a superposition of plane waves in the form

$$\bar{h}_{\mu\nu} = A_{\mu\nu} e^{ik_\alpha x^\alpha}, \tag{1.23}$$

where $A_{\mu\nu}$ is a constant symmetric tensor. Let us then consider a single plane wave.

Imposing the wave equation sets $k_\alpha k^\alpha = 0$, and the Hilbert gauge (1.11) condition can be written as $A_{\mu\nu} k^\mu = 0$, where $A = \eta^{\mu\nu} A_{\mu\nu}$.

In this framework we can impose the residual gauge condition explicitly: a function which satisfies $\Box \zeta_\mu = 0$ is $\zeta_\mu = B_\mu \exp(id_\alpha x^\alpha)$, where $d_\alpha$ is a null vector ($d_\alpha d^\alpha = 0$) while $B_\mu$ is a generic constant vector.

In these terms, the transformation equation (1.18) reads

$$\bar{h}_{\mu\nu} \to \bar{h}_{\mu\nu} + \left( -2iB_{(\mu} d_{\nu)} + i\eta_{\mu\nu} B_\beta d^\beta \right) e^{id_\alpha x^\alpha} \tag{1.24}$$

$$A_{\mu\nu} e^{ik_\alpha x^\alpha} \to A_{\mu\nu} e^{ik_\alpha x^\alpha} + \left( -2iB_{(\mu} d_{\nu)} + i\eta_{\mu\nu} B_\beta d^\beta \right) e^{id_\alpha x^\alpha}. \tag{1.25}$$

This tells us that if we set the vector $d_\alpha$ to be equal to $k_\alpha$ the amplitude $A_{\mu\nu}$ will transform according to the algebraic system

$$A_{\mu\nu} \to A_{\mu\nu} - 2iB_{(\mu} k_{\nu)}, \tag{1.26}$$

which allows us to impose four conditions on $A_{\mu\nu}$, one for each of the free components of $B_\mu$. It is customary to choose $A = 0 = A_{0i}$: these are known together as the transverse-traceless (TT) gauge.

The condition $A = 0$ also means that $h = 0 = \bar{h}$: thus, form this point onward we can stop distinguishing between $h_{\mu\nu}$ and $\bar{h}_{\mu\nu}$, and for simplicity's sake we write the former.

If we orient our axes such that $\vec{k} = k^i$ is along the $\hat{z}$ direction (which means $k^\mu = (k, 0, 0, k)^\top$) the conditions can be written as

1. Hilbert gauge + traceless: $A_{\mu 0} + A_{\mu 3} = 0$;

2. traceless: $A = -A_{00} + A_{11} + A_{22} + A_{33} = 0$;

3. transverse: $A_{0i} = 0$.

The Hilbert gauge combined with the transverse conditions show that $A_{00} = 0$ as well, followed by $A_{13} = 0$, $A_{23} = 0$ and $A_{33} = 0$.

Finally, the traceless condition imposes $A_{11} = -A_{22}$. These conditions tell us that the plane gravitational wave must have the form

$$
h_{\mu\nu}^{TT}(x) = \begin{bmatrix} 0 & 0 & 0 & 0 \\ 0 & h_+ & h_\times & 0 \\ 0 & h_\times & -h_+ & 0 \\ 0 & 0 & 0 & 0 \end{bmatrix} \exp(ik_\alpha x^\alpha), \tag{1.27}
$$

where $h_+ = A_{11}$ and $h_\times = A_{12}$.

In a later discussion we will use the fact that a general perturbation $h_{\mu\nu}$ can be *projected* into the TT gauge by using a certain projection tensor $\Lambda_{ijkl}$; this is not trivial to show, but the general idea follows from a decomposition of the full perturbation into scalar, vector and tensor components [Car19]. Specifically, the number of free components before gauge fixing is 4 scalar, 4 vector and 2 tensor components. The tensor components are gauge invariant, while the other 8 can each be separately set to zero in an appropriate gauge. After applying the same decomposition to the stress-energy tensor and writing the Einstein equations we find that the tensor perturbations (which are precisely the $h_+$ and $h_\times$ polarization degrees of freedom) are the only ones which propagate according to a wave equation. The projection, which yields a perturbation with two degrees of freedom, is thus only a way to recover the "radiative" part of the metric.

### 1.1.4 Effect on test masses

The TT gauge we defined has the rather peculiar characteristic of "moving with the wave", so that the position of any observer initially at rest (so, such that $u^\mu(\tau = 0) = (1, \vec{0})^\top$) is unchanged: the geodesic equation evaluated at $\tau = 0$ reads

$$
\left.\frac{d^2 x^\mu}{d\tau^2}\right|_{\tau=0} + \left.\Gamma^\mu_{\nu\rho} u^\nu u^\rho\right|_{\tau=0} = 0 \tag{1.28}
$$

$$
\left.\frac{d^2 x^\mu}{d\tau^2}\right|_{\tau=0} = -\Gamma^\mu_{00} = 0, \tag{1.29}
$$

since the Christoffel symbols computed $\Gamma^\mu_{00}$ with the TT gauge perturbation (1.27) all vanish: $\Gamma^\mu_{00} = \eta^{\mu\nu}(2g_{\nu0,0} - g_{00,\nu})/2 = 0$.

Does this mean that gravitational waves are merely an artefact, and have no effect on particles? No, since while in the TT gauge the *positions* of the points do not change, the *distance* among them does.

In order to understand this effect we can make use of the geodesic deviation equation [Car19, section 3.10], which states that if we take two geodesics whose four-velocities are both approximately $u^\mu$, separated by a short vector $\xi^\mu$,[3] they might diverge or converge, and the evolution of $\xi^\mu$ will be described by

$$\ddot{\xi}^\mu = R^\mu_{\nu\rho\sigma} u^\nu u^\rho \xi^\sigma .\tag{1.30}$$

Let us consider the same geodesics as before, whose four-velocity is uniformly $u^\mu \equiv \left(1, \vec{0}\right)^\top$: the "acceleration" will then be given by the matrix product $R^\mu_{00\sigma}\xi^\sigma$.

These components of the Riemann tensor read [Car19, eq. 7.106]:

$$R^\mu_{00\sigma} = \frac{1}{2}\ddot{h}^\mu_\sigma .\tag{1.31}$$

Therefore, the temporal component of the acceleration is $\ddot{\xi}^0 \propto \ddot{h}^0_\sigma = 0$, while the spatial components read

$$\ddot{\xi}^i = \frac{1}{2}\ddot{h}^i_j \xi^j .\tag{1.32}$$

These equations can then be explicitly solved. It is important to remark that $\ddot{\xi}^i$ is *not* co-ordinate acceleration: the points are *stationary* in the TT gauge coordinates, but the distance among them changes. Intuitively, we can interpret this as due to our carefully constructed gauge choice, which was determined through residual gauge, so it satisfied a wave equation $\Box \zeta_\mu = 0$: it precisely oscillates with the wave, allowing the position of any point to not change (to linear order). Fortunately GWs are physical, so they must still manifest regardless of our gauge, and they do so through the distortion of distances as described here.

The distances of points at a fixed position $(x, y, z)$ from the center change (up to a phase) according to the expression

$$x(t) = x_0\left(1 + h_+ e^{i\omega t}\right) + y_0 h_\times e^{i\omega t}\tag{1.33}$$

$$y(t) = y_0\left(1 - h_+ e^{i\omega t}\right) + x_0 h_\times e^{i\omega t} ,\tag{1.34}$$

which is shown graphically in figure 1 for four configurations: only $h_+$ or $h_\times$ being nonzero, or only $h_R \propto h_+ + ih_\times$ or $h_L \propto h_+ - ih_\times$ being nonzero. The last two are called *circular polarizations*.

---

[3] There is a technical note to be made here: in GR the notion of a vector between two points in the manifold is meaningless, however we can get around this problem by considering a one-parameter family of geodesics, and identifying the separation vector between them to be the tangent vector associated to the parameter.
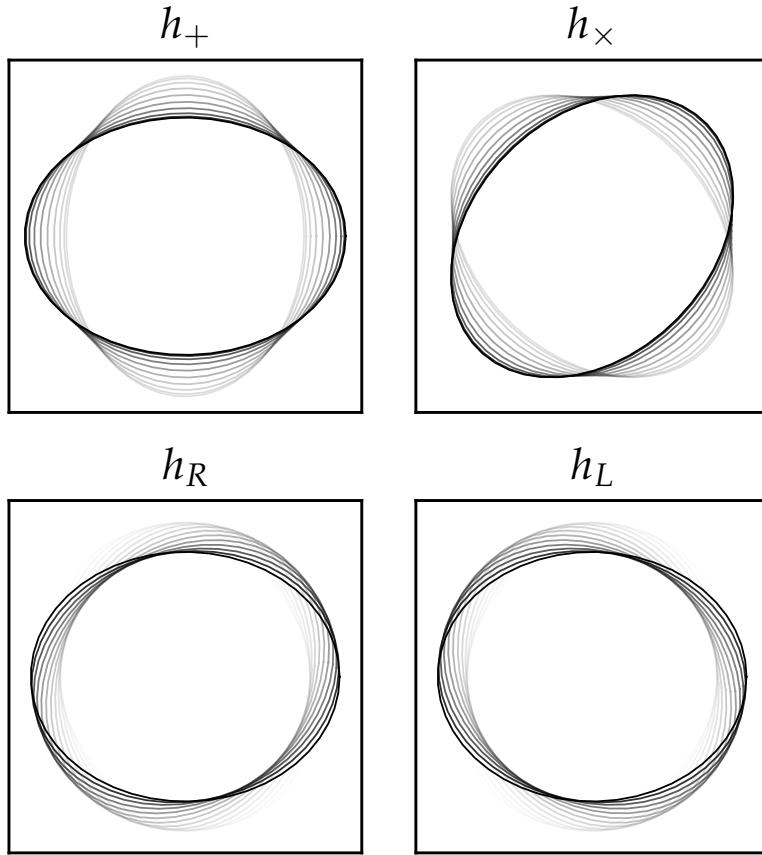
Figure 1: Polarizations of gravitational waves. Time evolution is represented though transparency: darker ellipses correspond to later points in time. The four cases are described in the text. We stress that in the TT gauge the ellipses do not represent changes in coordinate position but only in distance among points. In all cases the starting configuration is circular. The code generating this figure is available here.

This description is not the one an experimentalist might use: if we need to consider the noise due to other sources of gravitation, it is convenient to move from the TT gauge to the *proper detector frame*, in which the metric is expanded around a fiducial point of our detector — for instance, around the beam-splitter in an interferometer. In such a frame, it can be shown that the effect of GWs can be described as a Newtonian force on points a certain distance away from it — for instance, the mirrors of the interferometer. This comes in at second order in the distance, and it is given by [Mag07, eq. 1.96]

$$F_i = \frac{m}{2} \ddot{h}_{ij}^{TT} \xi^j \, , \tag{1.35}$$

which unsurprisingly closely mirrors the TT gauge variation of the distance: the physically measurable effect must be independent of gauge choice. The reason the TT gauge perturbation appears here as well is that the Riemann tensor, which is used in these computations, is

*invariant* (a stronger condition than covariant — the values of the components are actually unchanged) under gauge transformations.

### 1.1.5 The quadrupole formula

The lowest order contribution to the generation of gravitational waves can be calculated starting from the linearized Einstein equations (1.13). The Green's function method for the inversion of the D'Alambertian is a common technique: if we can find a function $G(z)$ such that $\Box G(z) = \delta^{(4)}(z)$, then we can do the following manipulation (denoting the gravitational constant as $G_N$ for clarity):

$$\Box_x \overline{h}_{\mu\nu}(x) = -16\pi G_N T_{\mu\nu}(x) \tag{1.36}$$

$$= -16\pi G_N \int \mathrm{d}^4 y\, T_{\mu\nu}(y)\delta^{(4)}(x-y) \tag{1.37}$$

$$= -16\pi G_N \int \mathrm{d}^4 y\, T_{\mu\nu}(y)\Box_x G(x-y) \tag{1.38}$$

$$= \Box_x \left( -16\pi G_N \int \mathrm{d}^4 y\, T_{\mu\nu}(y) G(x-y) \right) \tag{1.39}$$

$$\overline{h}_{\mu\nu} = -16\pi G_N \int \mathrm{d}^4 y\, T_{\mu\nu}(y) G(x-y) \tag{1.40}$$

$$= 4G_N \int \mathrm{d}^3 y\, T_{\mu\nu}(x^0 - |\vec{x}-\vec{y}|, \vec{y}) \frac{1}{|\vec{x}-\vec{y}|}, \tag{1.41}$$

Removing the D'Alambertian is valid insamuch as it will give us *a* solution for the wave equation, which will not be unique: $\Box f = \Box g$ does not imply $f = g$, but the reverse is true.

where in the last step we introduced the explicit expression for the Green's function of the D'Alambertian: $G(z) = -\Theta(z^0)/4\pi|\vec{z}|$ [Mag07, eq. 3.6].

We then have a formula for the trace-reversed perturbation, and as we discussed in section 1.1.3 far from the source we can recover the TT gauge perturbation by projecting this equation thanks to a tensor $\Lambda_{ij,kl}(\hat{n})$ (we return to $G \equiv G_N$ denoting the gravitational constant):

$$h_{ij}^{TT}(t,\vec{x}) = 4G\Lambda_{ij,kl}(\hat{n}) \int \frac{\mathrm{d}^3 y}{|\vec{x}-\vec{y}|} T_{kl}\left( t - |\vec{x}-\vec{y}|, \vec{y} \right), \tag{1.42}$$

where the tensor $\Lambda$ is constructed to be a projector which sends 2-tensors into the subspace of traceless tensors, which are transverse to the direction defined by $\hat{n} = \vec{x}/|\vec{x}|$:

$$\Lambda_{ij,kl} = P_{ik}P_{jl} - \frac{1}{2}P_{ij}P_{kl} \qquad \text{where} \qquad P_{ij} = \delta_{ij} - n_i n_j. \tag{1.43}$$

This expression can be further simplified by making use of the assumption that the source is far away: the integral over $\mathrm{d}^3 y$ ranges over a region which has a maximum size of $R$, the scale of the source, while the wave is observed at a distance $r = |\vec{x}| \gg R$. This allows

us to expand and neglect terms of the order $R^2/r^2$ and over;[4] the result we get is

$$h_{ij}^{TT} = \frac{4G}{r} \Lambda_{ij,kl}(\hat{n}) \int \mathrm{d}^3y\, T_{kl}\left(t - r + \vec{y} \cdot \hat{n}, \vec{y}\right). \tag{1.45}$$

This equation uses the stress-energy tensor as computed without considering the higher-order effects of gravity on matter (this is the meaning of "linear" in the linear wave equation (1.13)); thus it is only a good approximation in the case of objects whose typical scale $R$ is much larger, than, say, their Schwarzschild radius $2GM$. The problem with this assumption is that it fails to hold precisely for the sources which we are most interested in since, as we shall see, they give out some of the most easily detectable gravitational radiation: binary compact objects near coalescence.[5]

For a gravitationally bound source like a binary, with total mass $M$, reduced mass $\mu$, moving with speed $v$ and with a relative separation $r$, the virial theorem dictates that

$$\frac{1}{2}\mu v^2 = \frac{1}{2}G\frac{\mu M}{r} \implies v^2 = \frac{GM}{r} = \frac{R_s}{r}, \tag{1.46}$$

where $R_s$ is the Schwarzschild radius corresponding to the total mass of the system.

This means that the source not being very compact[6] ($R_s \ll r$) is equivalent to it moving slowly ($v \ll 1$). Neither of these assumptions will hold in the end, but since we are using one we should use both.

In Fourier space, this amounts to saying that the typical frequencies $\omega$ for which the amplitude of the Fourier transform of the stress-energy tensor is large will satisfy $\omega \vec{y} \cdot \hat{n} \lesssim \omega R \ll 1$. This means that we can expand the exponential in the Fourier transform; in the time domain this amounts to expanding in time around the retarded time $t - r$:

$$T_{kl}(t - r + \vec{y} \cdot \hat{n}, \vec{y}) \approx T_{kl}(t - r, \vec{y}) + \vec{y} \cdot \hat{n} \partial_t T_{kl} + \frac{1}{2}(\vec{y} \cdot \hat{n})^2 \partial_{tt}^2 T_{kl} + \mathcal{O}\left((\vec{y} \cdot \hat{n})^3\right). \tag{1.47}$$

This allows us to write the resulting wave as a multipole expansion:

$$h_{ij}^{TT}(t, \vec{x}) = \frac{4G}{r} \Lambda_{ij,kl}\left(S_{kl} + \sum_{L=1}^{\infty} \frac{1}{L!} \partial_t^L S_{kl|i_1 \dots i_L} n_{i_1} \dots n_{i_L}\right), \tag{1.48}$$

To be computed at redarded time.

where the moments of the stress tensor $S_{kl|i_1 \dots i_L}$ are defined as

$$S_{kl|i_1 \dots i_L} = \int \mathrm{d}^3y\, T_{kl} y_{i_1} \dots y_{i_L}. \tag{1.49}$$

---

[4] Specifically, we expand

$$|\vec{x} - \vec{y}| = \sqrt{x^2 + y^2 + 2x \cdot y} = r\sqrt{1 - 2\frac{\hat{n} \cdot \vec{y}}{r} + \frac{y^2}{r^2}} \approx r\left(1 - 2\frac{\hat{n} \cdot \vec{y}}{r} + \mathcal{O}\left(R^2/r^2\right)\right). \tag{1.44}$$

[5] As we shall discuss later, the amplitude of the waves emitted rises as they get closer and closer; also, BNSs and binary black holes (BBHs) often reach their peak amplitude in the frequency range where our detectors are most sensitive. Nevertheless, the "Newtonian" stage of the inspiral (a long time before the merger) will be described quite well by the expressions discussed here.

[6] We are being loose with terminology: the two stars in the binary may be compact themselves, but the system as a whole isn't.

We can also analogously calculate moments for the energy density $T_{00}$, which we denote $M_{i_1...i_L}$, and for the momentum density $T_{0i}$, which we denote $P_{k|i_1...i_L}$.

With integration by parts combined with the (flat space!) conservation of the stress-energy tensor $\partial_\mu T^{\mu\nu} = 0$ we can relate the $M$, $P$ and $S$ with equations such as [Mag07, eqs. 3.45–51]

$$\dot{M} = 0 \tag{1.50}$$

$$\dot{P}_i = 0 \tag{1.51}$$

$$\dot{M}_{ij} = 2P_{(i|j)} \tag{1.52}$$

$$S_{ij} = P_{i|j}, \tag{1.53}$$

where dots denote time derivatives.

These all tell us something interesting: $\dot{M} = 0$ and $\dot{P}_i = 0$ are energy and momentum conservation, which seem to tell us that there is no energy nor momentum loss from GW emission. This is an artifact, due to the assumptions of linear theory which neglect back-action on the source; fortunately we will still be able to compute the energy loss of the system even in this approximation.

The second useful fact is $S_{ij} = \ddot{M}_{ij}/2$: this allows us to write the lowest-order approximation of the expression of the wave from the source in terms of moments (1.48) as

$$h_{ij}^{TT}(t, \vec{x}) = \frac{2G}{r} \Lambda_{ij,kl} \ddot{M}_{kl}, \tag{1.54}$$

where

$$M_{kl}(t - r) = \int d^3y\, T_{00}(t - r, \vec{y}) y_k y_l. \tag{1.55}$$

since this expression only depends on the trace-free part of the moment $M$ we can write it as a function of the traceless **quadrupole moment**

$$Q_{kl} = M_{kl} - \delta_{kl} M_{nn}/3 = \int d^3y\, \rho(t, \vec{y}) \left( y^i y^j - \frac{1}{2} \delta^{ij} y^2 \right). \tag{1.56}$$

This gives rise to the quadrupole formula

$$h_{ij}^{TT}(t, \vec{x}) = \frac{2G}{r} \Lambda_{ij,kl} \ddot{Q}_{kl}(t - r). \tag{1.57}$$

### 1.1.6 Energy loss through gravitational radiation

The problem of quantifying the energy carried by gravitational radiation is thorny: first of all, there is no universally valid way to split the perturbation from the background in the general case; also, at each point we can always apply the equivalence principle to recover flat spacetime up to first order. It is impossible to construct a *local*, gauge invariant stress-energy tensor $T_{\mu\nu}^{GW}$ for GW radiation: the limit of the energy density contained in any volume will always vanish as that volume goes to zero.

However, we *can* define a tensor through an averaging procedure over many wavelengths and periods of the wave. There are different ways to do so, but a common one is the Landau-Lifshitz pseudotensor:

$$t_{\mu\nu} = -\frac{1}{8\pi G} \left\langle R^{(2)}_{\mu\nu} - \frac{1}{2}\overline{g}_{\mu\nu}R^{(2)} \right\rangle_{\text{mesoscopic}} \tag{1.58}$$

$$= \frac{1}{32\pi G} \left\langle \partial_\mu h_{\alpha\beta} \partial_\nu h^{\alpha\beta} \right\rangle , \tag{1.59}$$

where $R^{(2)}_{\mu\nu}$ and $R^{(2)}$ are the components of the Ricci tensor and scalar which are quadratic in the perturbation $h_{\mu\nu}$; $\overline{g}_{\mu\nu}$ is the background metric, and the averaging procedure is done on scales (wavelengths/periods) which are (much) larger than the typical wavelengths of the gravitational radiation considered, but (much) smaller than the typical wavelengths of the background [Mag07, sections 1.4.2, 1.4.3].

This pseudotensor can be used to describe the way in which, on large enough scales, the presence of GWs does indeed curve spacetime. Also, we can compute the energy flux passing through a surface a large distance from the source: if we use the quadrupole formula (1.57) for the gravitational perturbation, we can give an expression for the emitted power in terms of the third derivatives of the quadrupole as [Mag07, eq. 3.98]

$$\frac{\mathrm{d}E}{\mathrm{d}t} = -\frac{G}{5} \left\langle \dddot{Q}_{ij} \dddot{Q}_{ij} \right\rangle . \tag{1.60}$$

Dimensionally, $Q \sim \int \mathrm{d}^3 y \, \rho r^2$ has units of $\text{kg}\,\text{m}^2$; so $\dot{Q}$ has units of $\text{kg}\,\text{m}^2/\text{s}^3 = \text{W}$.

This means that the prefactor, which we wrote using $c = 1$, must really be $Gc^n/5$ with units of inverse power, which implies $n = -5$. Numerically, it is the inverse of $5c^5/G \approx 2 \times 10^{53}\,\text{W}$. This means that in order for GW emission to be efficient we must have a large value for $\dddot{Q}$: let us estimate it in terms of the typical size of the system, $R$, of its typical velocity $v = \Omega R$ and of its mass $M$. Each time derivative will roughly correspond to multiplication by a factor $\Omega$, so $\dddot{Q} \sim \Omega^3 M R^2 = v^3 M/R$.

The power can then be estimated as

$$-\frac{\mathrm{d}E}{\mathrm{d}t} \sim \frac{G}{5c^5}v^6\frac{M^2}{R^2} = \underbrace{\frac{1}{5}\frac{c^5}{G}}_{\sim 10^{52}\,\text{W}} \left(\frac{v}{c}\right)^6 \left(\frac{GM}{c^2 R}\right)^2 , \tag{1.61}$$

which tells us that the most significant sources of GW will be relativistic and compact. This prediction has been validated in 2015 with the first detection of GW from a BBH system [LIG+16], and again in 2017 with the first detection of GW from a BNS system [Abb+17].

## 1.2 Compact binaries

We focus our attention towards a pair of inspiraling (compact) objects, which we will initially model as point masses in quasi-circular orbits. The first thing we need to do is to

write an expression the amplitudes in the two polarizations $h_{+,\times}$ of the waves generated by a generic mass distribution with a mass moment $M_{ij}$ [Mag07, eqs. 3.67–68]:[7]

$$h_+(t, \hat{n}) = \frac{G}{r}\left(\ddot{M}'_{11} - \ddot{M}'_{22}\right) \tag{1.62}$$

$$h_+(t, \hat{n}) = \frac{G}{r}\left(2\ddot{M}'_{12}\right), \tag{1.63}$$

where $M'_{ij}$ are the components of the mass moment tensor in a frame whose $z'$ axis is aligned to the observation direction.

This frame is not the natural one with which to describe a binary system: typically, we would want to align the $z$ axis of the coordinates with the rotation axis. The rotation matrix between two systems depends on two angles, however one of these is more important than the other: aligning the $z$ axes can be accomplished by a rotation of angle $\iota$ (dubbed the *inclination*), while another rotation of angle $\phi$ is needed in order to align the $x$ and $y$ axes as well. However, since the system is rotating around its axis in a quasi-circular orbit, the second rotation only amounts to a time shift, an additional phase term in the oscillatory functions. For simplicity, we will neglect this phase freedom here and only include a variable phase at the end of the computations.

If the position of the bodies in the center-of-mass frame is

$$\vec{x}(t) = R \begin{bmatrix} \cos(\Omega t) \\ \sin(\Omega t) \\ 0 \end{bmatrix}, \tag{1.64}$$

then the mass moments read $M_{ij} = \mu x_i(t) x_j(t)$ (where $\mu = m_1 m_2 / (m_1 + m_2)$ is the reduced mass of the system), and going through the computation yields [Mag07, eq. 3.332]

$$h_+(t) = \underbrace{\frac{4G\mu\Omega^2 R^2}{r}}_{A}\left(\frac{1 + \cos^2\iota}{2}\right)\cos(2\Omega t) \tag{1.65}$$

$$h_\times(t) = \underbrace{\frac{4G\mu\Omega^2 R^2}{r}}_{A}\cos\iota\sin(2\Omega t) \tag{1.66}$$

$$A = \frac{4}{r}\left(\frac{G\mathcal{M}_c}{c^2}\right)^{5/3}\left(\frac{\pi f_{\text{gw}}}{c}\right)^{2/3}. \tag{1.67}$$

Approximating the motion of the bodies as circular during an orbit is called the *adiabatic approximation*, since it assumes that no energy is lost in each orbit (as that would deform the circle). The variation of the orbital frequency $\Omega$, which we shall compute shortly, must satisfy $\dot{\Omega} \ll \Omega^2$. It is a rather good approximation for the early stages of the inspiral, as we shall see.

---

[7] We could also write these in terms of the traceless quadrupole moment $Q_{ij}$; we follow the convention set forward by Maggiore [Mag07].

The last expression we wrote for the amplitude of the emission reintroduces factors of $c$, and it is expressed in terms of the emission frequency $f_{gw} = \omega_{gw}/2\pi = \Omega/\pi$ and of the *chirp mass*

$$\mathcal{M}_c = \frac{(m_1 m_2)^{3/5}}{(m_1 + m_2)^{1/5}} = \nu^{3/5} M \qquad \text{where} \qquad \nu = \frac{\mu}{M}. \tag{1.68}$$

The parameter $\nu$ is called the *symmetric mass ratio*, and it takes values from $\nu \to 0$ (one mass vanishing) to $\nu = 1/4$ (equal masses).

### 1.2.1 Energy evolution

Combining equations (1.65) with the quadrupole emission formula (1.60) yields an expression for the emitted power

$$P = \frac{32}{5} \frac{c^5}{G} \left( \frac{G\mathcal{M}_c \omega_{gw}}{2c^3} \right)^{10/3}. \tag{1.69}$$

This allows us to describe the evolution of the orbit in this quasi-adiabatic context: the total energy of the binary system, by the virial theorem combined with Kepler's third law $\Omega^2 R^3 = GM$, reads

$$E = -\frac{Gm_1 m_2}{2R} = -\frac{Gm_1 m_2}{2} \frac{\Omega^{2/3}}{G^{1/3} M^{1/3}} = -\left( \frac{G^2 \mathcal{M}_c^5 \omega_{gw}^2}{32} \right)^{1/3}. \tag{1.70}$$

With these two expressions at hand, we can impose $P = -\dot{E}$, which we can write in the form $\dot{\omega}_{gw} \propto \omega^n$ for some $n$: since $\dot{E} \propto \omega_{gw}^{-1/3} \dot{\omega}_{gw}$, $n$ will be $11/3$, and the specific expression will look like

$$\dot{\omega}_{gw} = \frac{12}{5} \sqrt[3]{2} \left( \frac{G\mathcal{M}_c}{c^3} \right)^{5/3} \omega_{gw}^{11/3}. \tag{1.71}$$

This equation is in the form $\omega^{-11/3} \, d\omega = K \, dt$; integrating from point 0 to point 1 we find $3K(t_1 - t_0)/8 = \omega_0^{-8/3} - \omega_1^{-8/3}$; if we treat this as an initial value problem we can see that as $t_1$ increases there is only a finite "budget" on the right-hand side: when $3K(t_1 - t_0)/8 = \omega_0^{-8/3}$, $\omega_1^{-8/3}$ must go to 0 so $\omega_1$ must diverge. The divergence itself is unphysical since, besides corresponding to a breakdown of some of our approximations, it comes about when considering point masses, while compact objects have a finite size and at some point collide.

Nevertheless, the moment of divergence happens close enough to the actual merger of the objects, therefore it is useful to call it $t_c$ and to define a time coordinate as $\tau = t_c - t$. In terms of this, the solution to the equation reads

$$f_{gw}(t) = \frac{\omega_{gw}(t)}{2\pi} = \frac{1}{2\pi} \left( \frac{3K\tau}{8} \right)^{-3/8} = \frac{1}{\pi} \left( \frac{5}{256\tau} \right)^{3/8} \left( \frac{G\mathcal{M}_c}{c^3} \right)^{-5/8}. \tag{1.72}$$

15

This expression for $f_{\rm gw}$ can be substituted into the gravitational waveforms (1.65); we must also update the phase term, since $2\Omega t$ is the phase for a uniformly circular orbit: we will want to use integrate the angular velocity, to find

$$\Phi(t) = \int^t \omega_{\rm gw}(\widetilde{t})\,\mathrm{d}\widetilde{t} = 2\int^t \Omega(\widetilde{t})\,\mathrm{d}\widetilde{t} \tag{1.73}$$

$$= -2\left(\frac{5G\mathcal{M}_c}{c^3}\right)^{-5/8}\tau^{-5/8} + \mathrm{const}. \tag{1.74}$$

In terms of this, the amplitude in the two polarizations will read [Mag07, eqs. 4.31–32]

$$h_+(t) = \frac{1}{r}\left(\frac{G\mathcal{M}_c}{c^2}\right)^{5/4}\left(\frac{5}{c\tau}\right)^{1/4}\left(\frac{1+\cos^2\iota}{2}\right)\cos\Phi(t) \tag{1.75}$$

$$h_\times(t) = \frac{1}{r}\left(\frac{G\mathcal{M}_c}{c^2}\right)^{5/4}\left(\frac{5}{c\tau}\right)^{1/4}\cos\iota\sin\Phi(t). \tag{1.76}$$

As we will discuss, it is convenient to have expressions for the Fourier transforms of these. An analytic computation of the integrals is intractable, but we can make use of a technique known as stationary phase approximation (SPA), which is discussed in detail in appendix A. The final expressions for the Fourier-domain waveforms are equations (A.18).

### 1.2.2 Spherical harmonics decomposition

The waveform we described so far comes from the quadrupole of the mass distribution, but higher-order moments also generate GWs. In general, in units where $G = c = 1$, one can write the waveform as [Aji+11, eq. II.6]

$$h_+ + ih_\times = \frac{M}{r}\sum_{l=2}^{\infty}\sum_{m=-\ell}^{\ell} h_{\ell m}(t)_{(-2)}Y_{\ell m}(\iota,\varphi), \tag{1.77}$$

where the functions $_{-2}Y_{\ell m}$ are called *spin-weighted spherical harmonics*, a generalization of the regular spherical harmonics. The only assumption in this expression is the $1/r$ scaling of the amplitude of the waveform. The expansion parameters $h_{\ell m}$ are time-dependent and complex, and the spin-weighted harmonics depend on the orientation of the basis we choose (see Sky position and polarization).

The harmonics which give the largest contribution are the $2, 2$ and $2, -2$ ones, which are conjugates of each other.

At this point we can notice an interesting scaling property: in these units lengths, times, energies, masses and momentums have the same dimensions. What happens, then, if we rescale all these quantities by the same amount? This means we are mapping $M \to \alpha M$ and $r \to \alpha r$ in the previous expression, so we can see that the amplitude $h$ is preserved. This is consistent with a time rescaling of the time $t \to \alpha t$, as can be seen in equation (1.75), and with a rescaling of the frequency $f \to f/\alpha$, as can be seen in equation (A.18). The result also holds at higher orders than the quadrupole, as we will see by the parametrization of the waveform in section 1.4.1.

### 1.2.3 Parameters for a compact binary coalescence (CBC) waveform

The waveform we wrote explicitly depends on:

1. the chirp mass $\mathcal{M}_c$, defined in (1.68);

2. the distance $r$, which in a more general cosmological context should be replaced by the *luminosity distance $D_L$*;

3. the inclination $\iota$, which is the angle between the observation direction and the total angular momentum of the system.

These are only some of the parameters which must be considered when discussing a CBC. We will now discuss the full set of parameters which can be used to fully describe the binary system generating the waveform [BGB21, eq. 21].

**Arrival time and initial phase**  The time at which any given waveform arrives at Earth is arbitrary, as is the global phase of the waveform. In practice, one will typically analyze the output from a detector in batches, and in each of these the analysis will be performed in Fourier space. Therefore, it is relevant to see how the Fourier-domain waveform responds to a time and phase shift: what is the transform of $f(t - t_0)e^{i\varphi_0}$? It comes out to be

$$\int_{\mathbb{R}} f(t - t_0)e^{i\varphi_0}e^{i\omega t}\,\mathrm{d}t = e^{i\omega t_0 + i\varphi_0} \underbrace{\int_{\mathbb{R}} f(t - t_0)e^{i\omega(t - t_0)}\,\mathrm{d}(t - t_0)}_{\widetilde{f}(\omega)}, \tag{1.78}$$

so a time shift corresponds to the addition of a linear term to the phase, while the phase can be directly moved from the time to the frequency domain.

**Sky position and polarization**  The wave will be coming from a sky position, which we can describe with respect to a given coordinate system through two angles; it is convenient to use right ascension $\alpha$ and declination $\delta$. Also, the polarization of the gravitational waves can have an arbitrary angle with respect to the observation direction: we denote this angle as $\psi$.

In more technical terms, a general waveform arriving our detector will be a superposition of GWs in the TT gauge (1.27) with varying $\alpha$, $\delta$, $\psi$ as well as different frequencies; we can write it as [Mag07, eq. 1.58]

$$h_{ab}(t, \vec{x}) = \sum_{\text{pol}=+,\times} \int_{-\infty}^{\infty} \mathrm{d}f \int \mathrm{d}^2\hat{n}\, \widetilde{h}_{\text{pol}}(f, \hat{n}) e_{ab}^{\text{pol}}(\hat{n}, \psi) e^{-2\pi i f(t - \hat{n}\cdot\vec{x}/c)}, \tag{1.79}$$

where $\hat{n} = \hat{n}(\alpha, \delta)$ is the vector describing the propagation direction of a specific component — in the context of a CBC the distribution of the $e_{ab}^{\text{pol}}(\hat{n}, \psi)$ will include a Dirac delta centered on the position of the source in the sky, while this more general expression can be useful, for example, in the context of a stochastic gravitational wave background (SGWB).

The tensors $e_{ab}$ are basis tensors: in a frame where $\hat{n}$ and $\psi$ are chosen such that the $+$ polarization stretches the $x$ and $y$ axes, they read

$$e_{ij}^+(\hat{n} = \hat{z}, \psi = 0) = u_i u_j - v_i v_j = \begin{bmatrix} 1 & 0 & 0 \\ 0 & -1 & 0 \\ 0 & 0 & 0 \end{bmatrix} \tag{1.80}$$

$$e_{ij}^\times(\hat{n} = \hat{z}, \psi = 0) = u_i v_j + v_i u_j = \begin{bmatrix} 0 & 1 & 0 \\ 1 & 0 & 0 \\ 0 & 0 & 0 \end{bmatrix}, \tag{1.81}$$

where $u$ and $v$ are two unit vectors defining the polarization direction; they are always chosen to be orthogonal, so fixing the angle $\psi$ is enough to determine them both once we give $\hat{n}$.

The aforementioned expansion glosses over a technical issue: the three-dimensional Fourier transform of the TT gauge waveform is in the form $h_{ij}(x) \sim \int d^3k\, A_{ij}(k) e^{ikx}$, so in order to write it like we did we need to define

$$\frac{f^2}{c^3} A_{ij}(f, \hat{n}) = \sum_{\text{pol}=+,\times} \tilde{h}_{\text{pol}}(f, \hat{n}) e_{ij}^{\text{pol}}(\hat{n}), \tag{1.82}$$

where we reparametrized the wavevector $\vec{k}$ through frequency $f$ and direction $\hat{n}$, and exploited the decomposition $d^3k = k^2\, dk\, d^2\hat{n}$.

**Masses and mass ratio**  The waveform to the lowest order we described only depends on the chirp mass $\mathcal{M}_c$, but as we will see later at higher order there appears a dependence on the ratio of the two masses: $q = m_1/m_2$,. It is customary to fix one of the two masses to always be the largest, therefore constraining $q \lessgtr 1$; we choose the convention $q \geq 1$.

A possible parametrization for the two masses is $(\mathcal{M}_c, q)$, another is $(M, q)$: these are equivalent, but in the following work we will typically use the latter because of the aforementioned scaling property of the waveforms: we conventionally work with respect to the dimensionless frequency $Mf$ and the dimensionless time $t/M$ in order to have one less parameter. If need be, we will refer to a "conventional" mass of $M = 2.8 M_\odot$, but our results will be easily scalable to any $M$.

**Spin**  Compact objects can spin, and the spin of each of the two is a vector with three independent components. These vectors $\vec{S}_i$ have units of angular momentum, but they are typically rescaled as

$$\vec{\chi}_i = \frac{c\vec{S}_i}{Gm_i} \in [-1, 1] \text{ in magnitude}. \tag{1.83}$$

The constraint of $|\chi_i| < 1$ can be approached by realistic models of BHs, while realistic models of NSs typically are constrained to spin much less, at the most $|\chi_i| \lesssim 0.7$ [LL11]. This constraint is hard to experimentally verify since one is faced with the degeneracy between

the components $\chi_{z,i}$ aligned with the direction of the angular momentum and the mass ratio $q$; in the analysis of the merger GW170807 two sets of prior distributions for the spins were used, $|\chi| < 0.05$ and $|\chi| < 0.89$, for this reason [Abb+17]. We have theoretical reasons to believe that the low-spins priors might correspond to a more physically meaningful scenario, but the degeneracy means that the high-spin case is not experimentally excluded, so we must still consider it a possibility.

The qualitative effect of spin is due to both spin-orbit and spin-spin interactions.

In the simplest spin-aligned case, $\vec{\chi}_i \propto \vec{L}$, the effect is to make the interaction less attractive (when the spins are aligned, $\vec{\chi}_1 \cdot \vec{\chi}_2 > 0$) or to make it more attractive in the alternate case.

The dynamics when the spins are not aligned are significantly more complicated, since the spins precess and give rise to modulations of the amplitude. Because of this, often models restrict themselves to the aligned-spin scenario.

**Tidal polarizability of neutron stars** If our compact objects are not black holes, they might be able to deform. The astrophysically motivated scenario we think of is that of neutron stars, but the following characterization could also apply to any extended compact objects. For concreteness' sake, we will refer to NSs.

This is a complicated process, but we can try to capture its most significant part by limiting ourselves to the quadrupole order of the deformation of the star. The discussion of this effect is clearest in the Newtonian context, but it can be also formalized in general relativity (GR) [Mag18, section 14.4.1].

Tidal effects are described by the tidal tensor $\mathcal{E}_{ij} = -\partial_i \partial_j U$, the traceless[8] Hessian of the Newtonian potential $U$. In the weak-field relativistic case, this corresponds to part of the Riemann tensor: $\mathcal{E}_{ij} = c^2 R_{0i0j}$.

We can describe the effects on the deformed star of such a tidal stress by looking at its quadrupole moment $Q_{ij}$ (see equation (1.56)). To linear order and neglecting any time dependence, we will have the relation

$$\mathcal{E}_{ij} = -\lambda Q_{ij}. \tag{1.84}$$

This parameter $\lambda$ describes the deformability of the star; if it is smaller the star deforms less in response to tidal perturbations. In practice the parameter used is not $\lambda$ itself but one of two common ways to rescale it: the $\ell = 2$ (quadrupole) **Love number**

$$k_2 = \frac{3}{2} \frac{G\lambda}{R^5}, \tag{1.85}$$

where $R$ is the radius of the deformed neutron star (NS), or the **tidal deformability**

$$\Lambda = \frac{2}{3} k_2 \left( \frac{Rc^2}{Gm} \right)^5, \tag{1.86}$$

---

[8] This tidal tensor describes the effect of one star's gravitational field on the other, so its source is not where we compute it, which is a convoluted way of saying that it should be taken to be a solution of $\nabla^2 U = 4\pi\rho$ in vacuum: therefore, $\nabla^2 U = -\text{Tr}\left[\mathcal{E}_{ij}\right] = 0$.

where $m$ is the mass of the deformed NS. The value of these parameters depends on the specific equation of state used in the model; $k_2$ is typically of the order of $10^{-1}$, and in the expression for $\Lambda$ we have a fifth power of the *compactness* $\sigma = Rc^2/Gm$ of the NS — this is expected to be a small number, but larger than 3,[9] so its fifth power will be of order $10^{3 \div 4}$. This means that the deformability $\Lambda$ will typically be of the order $10^{2 \div 3}$.

The Love number is useful since it is an expansion parameter for the gravitational field of the deformed NS. This field has contributions from both its own quadrupole moment, which is due to the tidal deformation from the other star, and from the gravitational field of the other star itself, which we can expand in terms of the tidal field around the center of the deformed star: $U_{\text{ext}} \approx -\mathcal{E}_{ij}x_i x_j/2$.

The gravitational field of the deformed star also changes under the effect of the deformation: including the first term in its expansion, which depends on the quadrupole moment, the potential reads

$$U_{\text{int}} \approx \frac{Gm}{r} + \frac{3G}{2r^3} \frac{x_i}{r} \frac{x_j}{r} Q_{ij} , \tag{1.87}$$

where $r = |x|$ is the radius from the center of the deformed star.

We can then see that under the assumption of linear dependence of the quadrupole on the tidal tensor the two potentials can be added (since we are still in the realm of linear theory):[10]

$$U \approx \frac{Gm}{r} - \frac{1}{2}\mathcal{E}_{ij}x_i x_j \left[ 1 + 2k_2(R/r)^5 \right] . \tag{1.88}$$

This is the starting point for the relativistic generalization of the result as well, where $k_2$ is an expansion parameter for a metric component.

The meaning of $\Lambda$ is less immediate — the first correction to the phasing of the waveform which appears is[11] [Mag18, eq. 14.231; FH08]

$$\Delta\Psi_{\text{5PN}}^{\text{tidal}} = -\frac{117}{256}\frac{m^2}{m_1 m_2}\widetilde{\Lambda}\left(\frac{v}{c}\right)^5 \qquad \text{where} \qquad \widetilde{\Lambda} = \frac{16}{13}\frac{(m_1 + 12m_2)m_1^4\Lambda_1 + (m_2 + 12m_1)m_2^4\Lambda_2}{(m_1 + m_2)^5} . \tag{1.89}$$

The parameter $\widetilde{\Lambda}$, which depends on the tidal deformabilities of the two stars $\Lambda_{1,2}$, is called the *reduced tidal parameter*.

One would expect to see $\Lambda = 0$ for black holes, and this is true in the nonspinning case; on the other hand, Kerr black holes can exhibit small but nonvanishing deformability. Le Tiec and Casals [LC21] recently showed that, for example, BHs with dimensionless spins of the order $\chi \sim 0.1$ can exhibit Love numbers on the order of $k_\ell \sim 2 \times 10^{-3}$, around two orders of magnitude less than NS values. The effect this will have on GW emission is yet to be determined, but one can suspect it will be small.

---

[9] A limit on the maximum redshift of radiation from the surface of a NS was calculated by Lindblom [Lin84] under the assumptions of causality and stability for the nuclear matter, which is equivalent to a compactness limit of $\sigma \geq 2.83$ [LP07].

[10] A technical fact to remember here is that the expansions do not naturally match: the expansion of the internal potential is in orders of $1/r$, while the expansion of the external one is in orders of $r$.

[11] The meaning of the PN expansion and of the expansion in orders of $v/c$ will be discussed in section 1.4.1.

**Eccentricity**   A general binary system will orbit in an ellipse with eccentricity $e \in [0, 1)$; the two semiaxes of the ellipse read [Mag07, eqs. 4.51]

$$a = \frac{R}{1 - e^2} \qquad \text{and} \qquad b = \frac{R}{\sqrt{1 - e^2}} \, . \tag{1.90}$$

It can be shown that, for a Keplerian orbit, the semimajor axis $a$ and the eccentricity $e$ depend on the total energy $E$ and angular momentum $L$ as [Mag07, eqs. 4.50, 4.53]

$$e = \sqrt{1 + \frac{2EL^2}{G^2 m^2 \mu^3}} \qquad \text{and} \qquad a = \frac{Gm\mu}{2|E|} \, . \tag{1.91}$$

In order to fully describe the GW emission from a binary system we must then also account for eccentricity; this parameter can also change as time progresses, and in order to describe this process we need a second evolution equation. This can be found thanks to the quadrupole angular momentum emission formula, which is analogous to the energy emission one (1.60) [Mag07, eq. 3.99]:[12]

$$\frac{\mathrm{d}L^i}{\mathrm{d}t} = -\frac{2G}{5c^5} \epsilon^{ikl} \left\langle \ddot{M}_{ka} \dddot{M}_{la} \right\rangle \, . \tag{1.92}$$

This allows us to make a system of two equations, $\mathrm{d}E/\mathrm{d}t$ and $\mathrm{d}L/\mathrm{d}t$, which we can reparametrize as equations for $\dot{a}$ and $\dot{e}$ [Mag07, eqs. 4.116–17]:

$$\dot{a} = -\frac{64}{5} \frac{G^3 \mu m^2}{c^5 a^3} \frac{1}{(1 - e^2)^{7/2}} \left( 1 + \frac{73}{24} e^2 + \frac{37}{96} e^4 \right) \tag{1.93}$$

$$\dot{e} = -\frac{304}{15} \frac{G^3 \mu m^2}{c^5 a^4} \frac{e}{(1 - e^2)^{5/2}} \left( 1 + \frac{121}{304} e^2 \right) , \tag{1.94}$$

which can be (nontrivially) analytically solved, yielding the result shown in figure 2.

It can be clearly seen that eccentricity will decrease as the semimajor axis shrinks due to GW emission. Typical astrophysical binaries need to shrink by several orders of magnitude before merging — the notorious pulsar in a binary system detected by Hulse and Taylor [HT75] has a semimajor axis of $a \approx 2 \times 10^9$ m and an eccentricity of $e \approx 0.617$, while the frequency of the GWs it emits is $f_{\mathrm{gw}} = 2/P \approx 7 \times 10^{-5}$ Hz [TW82].

If we were to wait until this reached a frequency range where next generation ground-based detectors might hope to detect it, $f \sim 10$ Hz, we would expect to see (using Kepler's third law $a^3 f^2 = \text{const}$) a reduction of semimajor axis by a factor $\sim 2700$: it would go off-scale to the left in figure 2, and we would expect to basically have $e \approx 0$. One can then see that this result holds for all but the most extreme initial values of $e$.

This is the reason why eccentricity is often not considered in GW modelling, while it is of crucial importance in astrophysical population studies, since it has a large effect on the emitted power (enhancing it) in the early stages of the inspiral.

---

[12] The angular momentum emitted in this expression is considered to be both spin and orbital angular momentum.
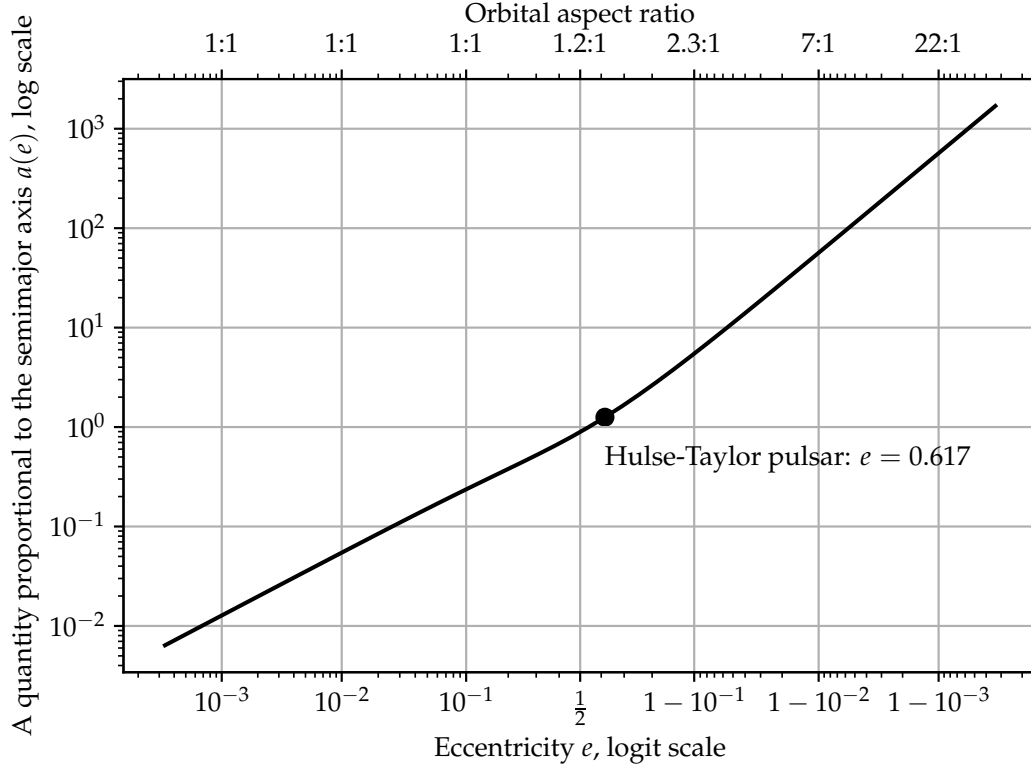
Figure 2: We show the behaviour of the analytic solution for the semimajor axis $a(e)$ [Mag07, eq. 4.126]; the $x$ axis is on a logit scale, meaning that it is proportional to $\log(e/(1-e))$. The quantity on the $y$ axis is not $a(e)$, but $a$ is proportional to it: ratios in the form $a(e_1)/a(e_2)$ are correctly represented in this graph.

Eccentric binaries are by no means excluded by this line of argument; there are astrophysical contexts in which they might be generated with high eccentricities combined with already small radii, which would allow $e > 0$ to be detectable even in the laser interferometer gravitational-wave observatory (LIGO)-Virgo band. Eccentric binary GW models do exist [Fav+21], and ignoring eccentricities may lead to bias in parameter estimation.[13]

**Summary**  The parameter vector $\vec{\theta}$ describing a binary system can be divided into internal and external parameters as

$$\vec{\theta} = (\underbrace{M, q, \vec{\chi}_1, \vec{\chi}_2, \Lambda_1, \Lambda_2}_{\theta_{\text{int}}}, \underbrace{D_L, \iota, \alpha, \delta, \psi, t_0, \phi_0}_{\theta_{\text{ext}}}), \tag{1.95}$$

where the dependence of the waveform on the external parameters is well-understood and easy to analytically calculate, while the dependence on the internal parameters (barring $M$)

---

[13] It is interesting to note that these models reach into "relativistic territory", and therefore must also include effects such as periastron precession — a good resource on these, based on [Fav11], is the https://www.soundsofspacetime.org/elliptical-binaries.html website, which also provides audio renditions of the waveforms.

is complicated.

The model developed in this work is built to reconstruct the dependence on $q$, $\Lambda_1$, $\Lambda_2$ and the aligned-spin components $\chi_{1,z}$ and $\chi_{2,z}$.

## 1.3 Interferometers and data analysis

Having seen how a gravitational waveform from a CBC might look to lowest order, we move to a discussion of the detection of these waveforms with interferometric techniques.

The response of any detector to a GW is a[14] scalar output, which will be in the form

$$h(t) = D_{ij} h_{ij}, \tag{1.96}$$

where $D_{ij}$ is known as the *detector tensor*. We want to apply this expression to the generic one for a gravitational wave (1.79), which we can simplify by

1. removing the integral in $d^2\hat{n}$: in the case of a CBC this is an excellent approximation;

2. removing the dependence on $\vec{x}$: this is called the *short-arm* approximation, which is warranted by the fact that our detectors have arms with lengths $L \sim 3\,\mathrm{km}$ and are most sensitive for GW frequencies of $f \sim 100\,\mathrm{Hz}$, while the frequencies corresponding to $L$ are $f \sim 100\,\mathrm{kHz}$.[15]

This leads to the following expression for the observed signal:

$$h(t) = \sum_{\mathrm{pol}=+,\times} \underbrace{D^{ij} e_{ij}(\hat{n}, \psi)}_{F_{\mathrm{pol}}} \underbrace{\int_{-\infty}^{\infty} df\, \widetilde{h}_{\mathrm{pol}} e^{-2\pi i f t}}_{h_{\mathrm{pol}}(t)} \tag{1.97}$$

$$= F_+ h_+(t) + F_\times h_\times(t). \tag{1.98}$$

The *detector pattern functions* $F_{+,\times}$ can be computed explicitly; for a Michelson-Morley interferometer they read

$$F_+ = \frac{1}{2}\left(1 + \cos^2\theta\right) \cos 2\phi \cos 2\psi - \cos\theta \sin 2\phi \sin 2\psi \tag{1.99}$$

$$F_\times = \frac{1}{2}\left(1 + \cos^2\theta\right) \cos 2\phi \sin 2\psi + \cos\theta \sin 2\phi \cos 2\psi, \tag{1.100}$$

where $\theta$, $\phi$ are the two angles describing the direction the GW is coming from in a frame aligned with the axes of the detector — they will depend on the sky position of the source $(\alpha, \delta)$ as well as the orientation of the detector in space (which depends on well-known parameters such as its latitude, the orientation of the earth at each time and so on).

---

[14] Current interferometric detectors have a single scalar response because of their Michelson-Morley design with arms at 90°; planned detector such as the Einstein Telescope will exhibit multiple scalar inputs [Tea11, section 5.3.2]. The following analysis still applies, each scalar input can be treated analogously; having multiple (from one multi-output detector or from a network) is incredibly beneficial for the accuracy of measurements.

[15] It is actually possible to not use this approximation, and in fact it is advisable not to: modern interferometers use power recycling techniques, which allow for the effective length of the arms to be much longer than their physical one. In fact, the optimal detection strategy for any given GW frequency is to have a detector whose arms are a quarter of the GW wavelength long [Mag07, eq. 9.33] — this balances the effect of the deformation due to the GW changing sign during the time of flight of any specific photon with the "stacking" effect of the photon taking a longer path through the deformed space.

### 1.3.1 Matched filtering

We have seen how the GW signal will look to our detector: $h(t)$, but in practical experiments what we will measure will be in the form $s(t) = h(t) + n(t)$,[16] and typically the magnitude of the noise timeseries $n(t)$ will be much larger than the magnitude of the signal.

This poses an issue both for the detection of a signal and for the analysis of a signal which has been identified as such. The technique we will describe here, matched filtering, has applications in both branches of GW data analysis.

The idea is to define a *filter*, a map from the signal timeseries to $\mathbb{R}$, in such a way that its value is low if there is no signal, and it is high if there is a signal of a certain shape. A common choice because of its computational simplicity is a *linear* filter, written as

$$s(t) \to \hat{s} = \int \mathrm{d}t\, s(t) K(t) \tag{1.101}$$

for some filter function $K(t)$, which we can select arbitrarily. How can we determine the best choice of $K$? We want to maximize the *distinguishability* between true signals and random noise, which we can quantify through the signal-to-noise ratio (SNR):[17]

$$\mathrm{SNR} = \frac{\mathbb{E}(\hat{s}|\text{presence of } h)}{\sqrt{\mathrm{var}(\hat{s}|\text{absence of } h)}} = \frac{S}{N}, \tag{1.102}$$

where we compute the root of a variance for $N$ since if there is only noise we expect $\hat{s} = \int \mathrm{d}t\, n(t) K(t)$ to be a random variable.

In order to properly express this, let us discuss our assumptions about the statistical properties of the noise: the simplest noise we can characterize is

1. stationary: its statistical properties are unchanging in time. This is not true in real detectors, but if the variation is slow enough one can work with "local" properties, on the scale of hours or days.

2. zero-mean: $\langle n(t) \rangle = 0$; this can be enforced by subtracting an offset.

3. uncorrelated in Fourier space: this can be stated simultaneously with the definition of the variance of each Fourier component, which is expressed through the single sided **power spectral density (PSD)**[18] $\langle \tilde{n}^*(f) n(f) \rangle = \delta(f - f') S_n(f)/2$.

---

[16] The "noise" described here is not actually what is measured: the output of the detector is not $h(t)$ but it is a linear function of it — even without accounting for the technical details of the measurement, the quantity measured is the intensity of the light at the dark fringe of the detector, not directly $h$. Nevertheless, if we know the transfer function of the detector we can refer the measured noise to an "effective noise" $n(t)$, which would be the noise we would need to add to $h(t)$ in order to see the signal we see. This effective noise is what we will call $n$ hereafter.

[17] Properly speaking, this quantifies the distinguishability only under the assumption of zero-mean noise, otherwise we could make it arbitrarily large by adding a constant to $s(t)$.

[18] The distinction between the single- and double-sided PSD depends on whether we want to use negative frequencies in the integral to recover the variance at each time or not:

$$\langle n^2(t) \rangle = \int_0^\infty \mathrm{d}f\, S_n^{\text{single-sided}}(f) = \int_{-\infty}^\infty \mathrm{d}f\, S_n^{\text{double-sided}}(f). \tag{1.103}$$

Since the noise is real-valued, these two are simply related by $S_n^{\text{single-sided}} = S_n^{\text{double-sided}}/2$.

4. Gaussian: each Fourier component is normally distributed around zero, with a variance described by the PSD.

The PSD, as defined, has the dimension of an inverse frequency; since it describes a variance it is often useful to discuss its square root, the *spectral strain sensitivity*, or *amplitude spectral density* $\sqrt{S_n}$, with dimensions $1/\sqrt{\text{Hz}}$.

With these assumptions, we can write the SNR, moving to Fourier space, as [Mag07, eq. 7.45]

$$\frac{S}{N} = \frac{\int_{\mathbb{R}} df\, \widetilde{h}(f)\widetilde{K}^*(f)}{\sqrt{\int_{\mathbb{R}} df\, (S_n(f)/2)\left|\widetilde{K}(f)\right|^2}} = \frac{(u|h)}{\sqrt{(u|u)}}, \tag{1.104}$$

where we defined the **Wiener product** between two real-valued signals $a$ and $b$ as the Fourier-space expression [Fin92; Mag07, eq. 7.46]

$$(a|b) = 4\,\text{Re} \int_0^\infty df\, \frac{\widetilde{a}^*(f)b(f)}{S_n(f)}. \tag{1.105}$$

The reason for the presence of the real part is that we want this to match the previous expression, where we know the signal $S$ to be real-valued; the factor 4 is a combination of the factor of 2 in the definition of the PSD and the fact that we restrict the integral to positive frequencies only, using the fact that the negative-frequency part gives the same contribution for real-valued signals.

We also defined the modified filter $u$, which is defined so that its Fourier transform reads $\widetilde{u}(f) = \widetilde{K}(f)S_n(f)/2$, which allows the expression with the Wiener product to match the previous one.

This expression can then be written as $S/N = (\hat{u}|h)$, where $\hat{u} = u/\sqrt{(u|u)}$ This is then maximized by $\hat{u}$ parallel to $h$ with respect to the metric defined by the Wiener product: $\hat{u} \propto h$ means that

$$\widetilde{K}(f) \propto \frac{\widetilde{h}(f)}{S_n(f)}. \tag{1.106}$$

In other words, the best way to find a signal buried in noise is to scale the Fourier-domain expression for the filter by the amplitude of the noise.

**Whitening**   An alternative way to write the same expression is through the concept of *whitening*: if $S_n(f)$ is known, we can transform any signal $a(t)$ into

$$a_w(t) \qquad \text{such that} \qquad \widetilde{a}_w(f) = \frac{\widetilde{a}(f)}{\sqrt{S_n(f)/2}}. \tag{1.107}$$

In other words, we are mapping a signal into another signal where all the noise Fourier components are uniformly scaled: white noise.

In terms of the whitened signals, the Wiener product just reads

$$(a|b) = (a_w|b_w)_w = 2\,\text{Re} \int_0^\infty df\, \widetilde{a}_w^*(f)\widetilde{b}_w(f) = \int_{-\infty}^\infty dt\, a_w(t)b_w(t), \tag{1.108}$$

so it can also be computed in the time domain.

**Optimal SNR** The expression for the SNR, if we are using the optimal filter, is then (in terms of an arbitrary constant $C$):

$$\text{optimal SNR} = \frac{(Ch|h)}{\sqrt{(Ch|Ch)}} = \sqrt{(h|h)} = 4 \int_0^\infty \mathrm{d}f \frac{\left|\tilde{h}(f)\right|^2}{S_n(f)}. \tag{1.109}$$

Amplitude strain profiles, as well as Fourier transforms of signals, are often plotted with log-scales: in order to have an intuition for this quantity we can reframe it as

$$\text{optimal SNR} = \int_{-\infty}^{\infty} \mathrm{d}\log f \frac{h_c^2(f)}{h_n^2(f)} \tag{1.110}$$

Used
$\mathrm{d}\log f = \mathrm{d}f / f$.

$$h_c(f) = 2f\left|\tilde{h}(f)\right| \tag{1.111}$$

$$h_n(f) = \sqrt{fS_n(f)}, \tag{1.112}$$

where the quantities $h_c$ and $h_n$ are called the **characteristic strains** of signal and noise [MCB15, eqs. 17–19]. They are both dimensionless, the way this integral is expressed allows us to integrate "by eye": if we plot log-characteristic strain against log-frequency, the positive area between $h_c$ and $h_n$ will be proportional to the optimal SNR.

Alternatively, we can define an "amplitude signal strain spectral density":

$$\sqrt{S_h(f)} = 2\sqrt{f}\left|\tilde{h}(f)\right|, \tag{1.113}$$

which is comparable to $\sqrt{S_n(f)}$, in the sense that it also has units of $\text{Hz}^{-1/2}$.

**The (optimal) mismatch** The scalar product $(a|b)$ between waveforms allows us to define a distance between them which is meaningful in terms of their distinguishability in data analysis. Specifically, we use the fact that in any inner product space we can write the product as $(a|b) = \sqrt{(a|a)(b|b)} \cos\theta$, where $\theta$ can be interpreted as an angle between $a$ and $b$. Therefore, we can define the *fidelity*, or *mismatch* "distance":[19]

$$M(a, b) = 1 - \frac{(a|b)}{\sqrt{(a|a)(b|b)}} = 1 - \cos\theta. \tag{1.114}$$

This mismatch is computed among two waveforms with all of their parameters fixed; in practice, it is often useful to let the initial phase and coalescence time of the waveforms free to vary, and compute the *optimal mismatch*

$$\mathcal{F}(a, b) = 1 - \max_{\phi_0, t_0} \frac{(a|b(\phi_0, t_0))}{\sqrt{(a|a)(b|b)}}, \tag{1.115}$$

---

[19] This is not a distance in the mathematical sense: it does not satisfy the identity of indiscernible principle since $M(a, Ka) = 0$ for any constant $K$, and it does not satisfy the triangle inequality $M(a, b) \leq M(a, c) + M(b, c)$ — think, for example, of $a$ and $c$ at right angles to one another (so $M(a, c) = 1$) and $b$ in the middle, at 45° from either, so $M(a, b) = M(b, c) = 1 - \sqrt{2}/2 \approx 0.3$. Then, $M(a, c) = 1 > M(a, b) + M(b, c) \approx 0.6$, in violation of the inequality.

This is not a problem for us: this mismatch is still a useful metric even if it is not a distance.

where either of the two waveforms is shifted in time and in phase.

In practice, this does not affect the norms of the waveforms in the denominator, but instead it means that the scalar product between $a$ and $b$ reads

$$\max_{\phi_0,t_0}(a|b(\phi_0,t_0)) = \max_{\phi_0,t_0} 4\,\mathrm{Re} \int_0^\infty \mathrm{d}f \, \frac{A_a(f)A_b(f)e^{i\phi_a-i\phi_b+2\pi i f t_0+\phi_0}}{S_n(f)} \tag{1.116}$$

$$= \max_{t_0} 4\left| \int_0^\infty \mathrm{d}f \, \frac{A_a(f)A_b(f)e^{i\phi_a-i\phi_b+2\pi i f t_0}}{S_n(f)} \right|. \tag{1.117}$$

This relation also means that while the mismatch $M(a,b)$ could in principle be as large as 2 (for $a(f) = -b(f)$) the optimal mismatch is bounded by 1, since there will always be a phase choice to make $(a|b)$ positive, albeit small in magnitude.

### 1.3.2 Parameter inference: studying the signal

Modern data analysis techniques for GW signals are Bayesian by necessity: we need to extract estimates for the parameters generating a signal of which we only have one measurement.

The quantity we want to extract from our analysis is the **posterior probability density function** $\mathbb{P}(\vec{\theta}|s)$, where $\vec{\theta}$ is the parameter vector while $s$ represents the data from the detector. If we integrate it in a certain hyper-volume $\Omega$, we get $\int_\Omega \mathrm{d}^n\vec{\theta}\,\mathbb{P}(\vec{\theta}|s)$: the answer to the question "given the data we measured, what is the probability that the parameters of the system were contained in the region $\Omega$?"

The way we write these probabilities is a compactification of notation: after the "given" symbol we should also always ideally include all the other assumptions about the signal, the noise, and the way they are combined into $s = h + n$. We will always leave this implicit, but we understand that the probabilities calculated will always be model-dependent.

A Bayesian approach starts by applying Bayes' theorem:

$$\underbrace{\mathbb{P}(\vec{\theta}|s)}_{\text{posterior}} = \frac{\mathbb{P}(s|\vec{\theta})\mathbb{P}(\vec{\theta})}{\mathbb{P}(s)} \propto \underbrace{\mathbb{P}(s|\vec{\theta})}_{\text{likelihood}} \underbrace{\mathbb{P}(\vec{\theta})}_{\text{prior}}, \tag{1.118}$$

where the reason we can neglect the dependence on $\mathbb{P}(s)$ is that it is a constant: since probability density functions are normalized to have unit integral over the whole space, we can worry about normalization in the end. Also, there are techniques to explore the posterior probability density space (such as Metropolis-Hastings (MH) sampling) which can use an unnormalized version of the posterior.

The prior, which encodes our prior belief about the potential values of the parameters, is often chosen to be uninformative,[20] so that we do not introduce bias in the analysis. In certain cases it might be warranted to use "biased" priors: for example, the analysis for

---

[20] This does not necessarily mean "uniform": there is a method, known as Jeffrey's prior, which allows one to maximize the "ignorance" about a parameter once a likelihood is given, through what is basically an argument for reparametrization invariance. For example, an uninformative prior on the mean of a Gaussian is uniform, while an uninformative prior on its standard deviation is log-uniform.

GW170817 offers results based on a low-spin and a high-spin prior [Abb+17]: the first is theoretically motivated and might be more meaningful, but the second is still allowed by the data.

The second ingredient is the likelihood $\mathbb{P}(s|\vec{\theta})$: this is where signal modelling comes in, since the likelihood needs to include the way the theoretical signal $h_\theta(t)$ depends on the parameters.

What is the probability of observing $s = h_\theta + n$ if we fix $\theta$? The theoretical signal $h_\theta$ can be computed and is thereafter fixed, likewise $s$, so this is just the probability of observing a certain realization of the noise: under the assumption of Gaussianity, it will read

$$\mathbb{P}(h_\theta + n|\vec{\theta}) \propto \exp\left(-\frac{1}{2}\int_\infty^\infty \mathrm{d}f \frac{|n(f)|^2}{S_n(f)/2}\right) \tag{1.119}$$

$$\propto \exp\left(-\frac{(n|n)}{2}\right) = \exp\left(-\frac{(s - h_\theta|s - h_\theta)}{2}\right) \tag{1.120}$$

$$\propto \exp\left((s|h_\theta) - \frac{(s|s)}{2} - \frac{(h_\theta|h_\theta)}{2}\right) \tag{1.121}$$

$$\propto \exp\left((s|h_\theta) - \frac{(h_\theta|h_\theta)}{2}\right). \tag{1.122}$$

This is a closed-form expression for our posterior probability density, so if computational power were no issue we would be done: the function $\mathbb{P}(\theta|s)$ includes all the possible information we could extract about the parameters from our observation. We can use *estimators* for single parameters and their variances in order to better understand what we have measured: these are functions which take the full posterior and return an estimate for a single quantity, such as the value for a specific parameter. These will always be a simplification of the true distribution, but they are very useful by virtue of being simple to understand.

We ask of these estimators that they be

1. consistent: they should converge to the true value as more data is included;

2. efficient: they should minimize the variance[21] of the estimate;

3. robust: they should not be very sensitive to small fluctuations in the posterior distribution.

A choice which satisfies these criteria quite well is the **Bayes estimator**, which estimates a parameter $\theta^i$ and the covariance matrix component $\Sigma_{ij}$ as

$$\hat{\theta}^i = \int \mathrm{d}^n\vec{\theta}\,\theta^i \mathbb{P}(\vec{\theta}|s) \tag{1.123}$$

---

[21] Here it is important to be careful: this is not the variance of the parameter, an estimate of the error we assign to it based on our single experiment, but the variance of the *estimates* taken over the space of possible experimental results we could have gotten while keeping the value of the true parameter fixed to a certain value

$$\hat{\Sigma}_{ij} = \int d^n\vec{\theta} \left(\theta^i - \hat{\theta}^i\right)\left(\theta^j - \hat{\theta}^j\right)\mathbb{P}(\vec{\theta}|s).\tag{1.124}$$

Depending on the way the posterior distribution is calculated and parametrized, computing this may be impractical. Other choices include estimating the parameters by the values which maximize the likelihood or the posterior, and the covariance from the Hessian of the probability density function (PDF) around that point.

So, how do we compute the posterior distribution $\mathbb{P}(\vec{\theta}|s)$ in practice? We know how to evaluate it at a single point $\vec{\theta}$, so we could evaluate it on some sort of grid, say, sampling $N$ equally spaced points in a reasonable interval for each parameter. The curse of dimensionality makes this infeasible: if we have $n$ parameters we would need $N^n$ evaluations; even with a very small $N \sim 10$ this quickly becomes unreasonably large, since we typically have $n \sim 15$ parameters.

One solution to this issue is to stochastically sample $\mathbb{P}(\theta|s)$, taking steps in randomly determined directions using a rule which includes information about the probability distribution. If the rule is appropriately selected, the sequence of points touched by this random walk will approximate a set of samples for the true distribution. This is known as **Monte Carlo** sampling. A common way to construct an appropriate rule is to make it memory-less, so that each new point is determined only based on the probability distribution and the current point. This is known as a **Markov Chain**.

Several algorithms implement Monte Carlo markov chain (MCMC) sampling; a common choice is the Metropolis-Hastings one, which is shown as algorithm 1; the function $p(\theta)$ should be chosen to be proportional to $\mathbb{P}(\theta|s)$ (the normalization is irrelevant), and we need to provide a probability density function $g(\theta_{\text{new}}|\theta)$ such that samples from $g$ can be easily be drawn. A common choice for $g$ is a Gaussian distribution centered in $\theta$, which has the advantage of being symmetric: $g(\theta_{\text{new}}|\theta) = g(\theta|\theta_{\text{new}})$. Further, we need a randomly chosen initial point $\theta_0$.

This random walk will eventually (for $N_{\text{samples}} \to \infty$) converge to the true distribution mathematically; there are several heuristics which can be used to check whether this is actually happening in a specific number of steps, such as measuring the autocorrelation of the chain, or running several chains starting at different points and checking that they "mix" appropriately.

## 1.4 Higher order waveforms

The treatment of GW production in linear gravity discussed in section 1.2 is useful but incomplete: as equation (1.61) shows, the systems emitting the most are *relativistic* ($v/c$ is large) and *compact* ($R_s/R$ is large). This has been verified in practice by the fact by the binary systems we detected: mostly BBHs, with some BNSs.

The quadrupole approximation, as well as the linearization of gravity, breaks down in the case we are interested in: what to do?

In the following sections we will discuss the main strategies[22] used to model CBC waveforms during all of their stages.

---

[22] One strategy which is not particularly relevant in this work but which is useful in other contexts is the gravitational self-force approach [Wal09], in which one works in orders of $m_1/m_2$, by making successive cor-

**Algorithm 1** Metropolis-Hastings algorithm.

---

**Require:** $p(\theta)$, $g(\theta_{\text{new}}|\theta)$, $\theta_0$, $N_{\text{samples}}$
    $i \leftarrow 0$
    $S \leftarrow \varnothing$
    **while** $i < N_{\text{samples}}$ **do**
        $\theta_{\text{new}} \leftarrow$ sample from $g(\theta_{\text{new}}|\theta_i)$
        $\alpha \leftarrow p(\theta_{\text{new}})/p(\theta_i) \times g(\theta_i|\theta_{\text{new}})/g(\theta_{\text{new}}|\theta_i)$
        with probability $\min(\alpha, 1)$ accept
        **if** accept **then**
            $\theta_{i+1} \leftarrow \theta_{\text{new}}$
        **else**
            $\theta_{i+1} \leftarrow \theta_i$
        **end if**
        $S \leftarrow S \cup \theta_{i+1}$
        $i \leftarrow i + 1$
    **end while**
    **return** sample set $S$.

---

Qualitatively, a waveform from a CBC involves a long *inspiral* phase which terminates when the two compact bodies *merge*, and finally a *ringdown* phase in which the single body remaining exhibits damped vibrations.

### 1.4.1 Post-Newtonian

The assumptions which we made in order to derive the quadrupole formula for the emission of gravitational radiation (1.57) were to consider a non-compact, slow-moving source ($v \ll c$), on a flat background.

One might wish to expand the equations of motion in orders of $v/c$, and this is the idea behind the PN expansion, but there are technical difficulties associated with this. In terms of notation, a $n$PN expansion will be up to order $(v/c)^{2n}$ in this work.

**Technical difficulties** The strength of the gravitational field scales with the ratio of the Schwarzschild radius of an object to the distance between the objects, so as the system becomes relativistic in speed the gravity also becomes strong. The flat background metric needs to be substituted; a common choice is a Post-Minkowskian expansion, which is an expansion in orders of $R_s/r$, where $R_s$ is the Schwarzschild radius for the combined system. This expansion and the PN one have different domains of validity (one far from the source, one near it), so one needs to find an *overlap region* and match them.

GWs of low order source higher-order ones, as well as back-reacting and subtracting energy from the source. The latter of these effects comes about at the 2.5PN order: equating

---

rections to geodesic motion in a fixed background. This is not applicable to neutron stars, whose mass ratios are never extreme, but it is useful to discuss extreme mass ratio inspirals.

the emitted power estimated in equation (1.61) to the derivative of the energy (which by the virial theorem has the same magnitude as the kinetic energy) $\dot{E} = -Mv\dot{v}$ we find $\dot{v} \propto (v/c)^5$.

We can expand the retarded-time argument of the stress-energy tensor, $t - r/c$, around $r = 0$; this, however, is only valid if we are relatively near the source and breaks down if we try to extend the result to the "radiation zone" where our detector lies — we need to treat that zone separately. This expansion allows us to express the Dalambertian as $\Box \approx \left(1 + \mathcal{O}\big((v/c)^2\big)\right)\nabla^2$, and to turn the Einstein equations into Poisson equations of the form

$$\triangle g^{(n)}_{\mu\nu} = \text{matter source} + \text{metric source from } g^{(n-1)}_{\mu\nu}. \tag{1.125}$$

After computing the $n$PN equations of motion we will need to compute the appropriate number of terms in the multipole expansion (1.48). This may also lead to divergencies: as we expand $\frac{1}{|\vec{x}-\vec{y}|}$ we get terms of type $(\vec{x}\cdot\vec{y})^\ell$ with large values for $\ell$, which rapidly diverge as we get further from the source. Specifically, the Poisson integrals, which solve $g(\vec{x}) = \nabla^2 f(\vec{x})$ with

$$f(\vec{x}) = -\frac{1}{4\pi}\int_{\mathbb{R}^3}\frac{d^3y}{|\vec{x}-\vec{y}|}g(\vec{y}) \tag{1.126}$$

will not always converge. Fortunately, this only reflects a limitation of the Poisson integral, and through analytic continuation one can recover a physical solution which respects the boundary conditions.

Solutions to these problems have been developed between the '80s and the early 2000s, and currently there exist general formalisms, such as the Blanchet-Damour, one which allow for high-order computations of PN waveforms [Bla14].

**PN waveforms** The typical notation used for PN waveforms expresses them [Mag07, sec. 5.6.1] as a function of the dimensionless frequency

$$x = \left(\frac{GM\Omega}{c^3}\right)^{2/3} = \mathcal{O}\big((v/c)^2\big), \tag{1.127}$$

$GM/r \sim v^2$ and $r\Omega \sim v$.

the symmetric mass ratio $\nu = \mu/M$ and the dimensionless time

$$\Theta = \frac{\nu c^3}{5GM}(t_c - t). \tag{1.128}$$

These are related by $x = \Theta^{-1/4}/4$ (a reframing of equation (1.72)) at Newtonian order, and we can also write the phase as

$$\phi - \phi_0 = -\frac{\Theta^{5/8}}{\nu} = -\frac{x^{-5/2}}{32\nu}. \tag{1.129}$$

Corrections to this expression are then written multiplicatively as a series in $x$ (or, really, in $x^{1/2}$, but the PN order is the exponent of $x$):

$$\phi - \phi_0 = -\frac{x^{5/2}}{32\nu}\left(1 + c_{1\mathrm{PN}}x + c_{1.5\mathrm{PN}}x^{1.5} + \ldots\right). \tag{1.130}$$

31

The error in the phase is therefore of order $x^{-1/2} \gg 1$ if we do not go beyond 2PN order: we need a high-order computation in order to recover an accurate expression for the phase. Current results include very high order waveforms, such as 5.5PN [BDG20].

**The PN order of tidal stresses**  We can give a crude estimate, which turns out to be accurate, for the PN order at which the effects of quadrupolar tidal deformation come in [Mag07, pagg. 288–289].

The quadrupole moment can be estimated as $Q_{ij} \sim \epsilon m r^2$ where $\epsilon$ is the induced ellipticity of the NS while $m, r$ is its mass and radius. This ellipticity comes from the tidal effect of the companion; it can be estimated as the ratio of the tidal force to the restoring self-gravity of the star:

$$\epsilon \sim \frac{F_{\text{tidal}}}{F_{\text{self}}} \sim \frac{Gmr/d^3}{Gm/r^2} = \left(\frac{r}{d}\right)^3 , \tag{1.131}$$

where $d$ is the separation between the two stars, and we assume that their masses are the same.

The inter-body force induced by the quadrupolar deformation depends on the quadrupole moment like [Mag07, eqs. 5.219, 5.235]

$$F_k^{\text{induced}} \approx Q_{ij} \partial_i \partial_j \partial_k U^{\text{Newton}} \sim \frac{Q_{ij}}{m} \partial_i \partial_j F_k^{\text{Newton}} \sim \left(\frac{r}{d}\right)^3 \frac{r^2}{d^2} F_k^{\text{Newton}} , \tag{1.132}$$

so $F^{\text{induced}} \sim (r/d)^5 F^{\text{Newton}}$. This ratio can be reframed in terms of $v/c$: the radius $r$ of a star is proportional to its Schwarzschild radius $Gm/c^2$; while the separation of the two is given by the virial theorem: $mv^2 \sim Gm^2/d$, so $d \sim Gm/v^2$. This means that

$$F^{\text{induced}} \sim (v/c)^{10} F^{\text{Newton}} , \tag{1.133}$$

and since the Newtonian order is the 0PN one tidal forces come in at 5PN order.

While this is a very high order, the dimensionless tidal deformability parameters $\Lambda$ are numerically large: therefore, it can be useful to include higher-order tidal terms in a lower-order calculation.

The effect of spin-orbit interactions, on the other hand, comes about at 1.5PN order, while spin-spin interactions are a 2PN effect.

### 1.4.2 Numerical Relativity

The PN expansion, even if it goes to high order, is still not enough when we approach the merger.

Thus, we need to compare our results to NR simulations, in which the spacetime metric and the stress-energy tensor are evolved according to the Einstein equations. This is possible but time-consuming: each simulation requires many days of supercomputer time.

The gravitational signal can be extracted from the simulated spacetime by computing the Weyl scalar $\Psi_4 = C_{\alpha\beta\gamma\delta} n^\alpha m^\beta n^\gamma m^\delta$,[23] where $n$ and $m$ are component vectors of a null

---

[23] Here $C_{\alpha\beta\gamma\delta}$ is the Weyl tensor, the fully traceless part of the Riemann tensor, whose definition can be found for example in Gourgoulhon [Gou07, eq. 2.18].

tetrad [Löf+12, sec. 5.6.3]. This scalar is related to gravitational wave emission by

$$\Psi_4 = \ddot{h}_+ - i\ddot{h}_\times . \tag{1.134}$$

The advantage is that we can incorporate the full machinery of GR, and account for the internal dynamics of neutron stars, as well as other phenomena such as the formation of an accretion disk after the merger [Ned+20].

Besides using the waveforms as validation for any model, an approach we can use for waveform generation is called "Inspiral-Merger-Ringdown (IMR) phenomenological": a PN waveform is complemented with a power series fitted to NR simulations [Kum+15]. Several variations on this idea are implemented in the LIGO Algorithm Library (LAL) [Col18].

### 1.4.3 Effective One Body

The EOB framework allows for the generation of waveforms encompassing inspiral, merger and ringdown, by mapping the relativistic two-body problem onto the motion of a test particle in an effective metric. This problem is described through an effective Hamiltonian, whose equations of motion are then numerically solved. Let us describe the procedure in a simplified case, including neither spin nor tidal interactions.

The Hamiltonian of the real system is approximated with a PN one, written in relative Arnowitt, Deser, Misner (ADM) coordinates and made dimensionless [Dam14, eqs. 4–5]:

$$\hat{H} = \frac{H}{\mu} = \underbrace{\frac{p^2}{2} - \frac{1}{q}}_{\text{Newtonian}} + \underbrace{\frac{1}{8}(3\nu - 1)(p^2)^2 - \frac{1}{2}\left[(3+\nu)p^2 + \nu(n \cdot p)^2\right] + \frac{1}{2q^2}}_{\text{1PN}} + \dots, \tag{1.135}$$

where $q$ and $p$ are dimensionless variables related to relative distance and the corresponding momentum by $q = rc^2/GM$ and $p = p'/\mu$, where $p'$ is the momentum with the correct dimensions.

This is then matched[24] to the Hamiltonian of a particle moving in an effective metric

$$g_{\text{eff}} = A(u,\nu)\,dT^2 + B(u,\nu)\,dR^2 + R^2\,d\Omega^2 \tag{1.136}$$

$$A(u,\nu) \approx 1 + \tilde{a}_1(\nu)u + \tilde{a}_2(\nu)u^2 + \dots \tag{1.137}$$

$$B(u,\nu) \approx 1 + \tilde{b}_1(\nu)u + \tilde{b}_2(\nu)u^2 + \dots, \tag{1.138}$$

where $u$ is the inverse radial coordinate $u = GM/c^2R$. The way to do so is to write both Hamiltonians in Delaunay (action-angle) coordinates. The metric potentials $A$ and $B$, to 3PN order, read:

$$A_{\text{3PN}} = 1 - 2u + 3\nu u^2 + \left(\frac{94}{3} - \frac{41\pi}{32}\right)\nu u^3 \tag{1.139}$$

---

[24] The way this "matching", this construction of a dictionary between the two- and the one-body problems, is performed is through a quantum-mechanical analogy. The idea is to consider the quantized energy levels corresponding to the classical Hamiltonians, which will depend on the quantum numbers $n$ (principal quantum number) and $\ell$ (total angular momentum), while the quantum number $m$, describing the $z$ component of the angular momentum, is irrelevant because of the spherical symmetry of the problem. One can then determine the correspondence by establishing a rule to translate between the energy levels corresponding to the same $(n, \ell)$ pairs [Dam14].

$$B_{3PN} = \frac{1 - 6\nu u^2 + 2(3\nu - 26)\nu u^3}{A_{3PN}}. \tag{1.140}$$

Note that the $\nu \to 0$ case corresponds to one of the masses vanishing: therefore, we are looking at a test particle in Schwarzschild geometry, and we indeed recover $A = 1 - 2u = 1/B$. The other extreme case is $\nu = 1/4$, which corresponds to $m_1 = m_2$.

A strategy which is then used is Padé resummation: the idea is to take a Taylor expansion (such as those for the PN potentials) and match it to a ratio of polynomial functions, so that

$$f^{(N)}(x) = \sum_{n=1}^{N} c_n x^n \approx P_L^M[f^{(n)}(x)] = \frac{\sum_{n=1}^{M} a_n x^n}{\sum_{n=1}^{L} b_n x^n}, \tag{1.141}$$

where the coefficients $c_n$ are fixed, while the $a_n$ and $b_n$ are determined algebraically by having equal-order terms match in the two series.

A Padé approximant $P_L^M$ can then be applied to any polynomial function. This may seem pointless, since it reproduces the PN result at the same order, however in practice the Padé-resummed expression often exhibits desirable behaviours, such as avoiding divergences or having faster convergence to the true potential.

The Hamiltonian whose equations of motion are actually solved is expressed in terms of the potentials [BB21, eq. 8.22]:

$$H_{EOB} = Mc^2 \sqrt{1 + 2\nu(\hat{H}_{eff} - 1)} \tag{1.142}$$

$$\hat{H}_{eff} = \frac{H_{eff}}{\mu} = \sqrt{A(u,\nu)\left(1 + p_\phi^2 u^2 + 2\nu(4 - 3\nu)u^2 p_{r*}^4\right) + p_{r*}^2}, \tag{1.143}$$

where $p_{r*} = \mu^{-1} \int (B/A) \, dR$ is the momentum corresponding to a rescaled radial variable, while $p_\varphi = P_\varphi/(\mu GM)$ is a rescaled angular momentum.

This formalism can then be complemented by including some further elements: one is the radiation reaction force, which can be expressed as an influence decreasing the momentum $p_\varphi$ according to the emitted flux. Including this term means we are not considering an *adiabatic* approximation anymore.

Further, next-to-quasi-circular terms are introduced: these are multiplicative corrections to the last orbits which account for the fact that these are getting further and further from being circular. Finally, the waveform is smoothly connected to a model for the ringdown, which is informed by black hole (BH) perturbation theory and NR simulations.

EOB models can also incorporate tidal and spin effects: the waveform model TEOBResumS [Nag+18] is applicable to spin-aligned, tidally interacting compact objects.

These EOB models can reproduce NR results quite well: for example, in the case of spinning BBH binaries Nagar, Bonino, and Rettegno [NBR21, fig. 2] find mismatches between the EOB and GWs from NR simulations to be at most of the order of $F \sim 10^{-2}$ and typically even less, $F \sim 10^{-3}$.

The EOB models natively output time-domain waveforms, while as discussed in section 1.3 we need them in the frequency domain in order to perform data analysis. One must therefore find a way to move to the frequency domain. An option is to use a SPA [GBN20];

this has been found to be quite successful in providing fast waveform evaluations even for low initial frequencies. However, it is still an approximation: ideally, we would want to numerically Fourier-transform the time-domain waveform. This becomes quite slow as we reach lower initial frequencies: the duration of the waveform for an equal-mass BNS with $M \approx 2.8 M_\odot$ is typically [Mag07, eq. 4.21]

$$\text{duration} \approx 3 \min \left( \frac{f_0}{20 \, \text{Hz}} \right)^{-8/3}. \tag{1.144}$$

In order to perform a fast Fourier transform (FFT), we need equally-spaced points in time, so the full duration needs to be densely sampled; also, the merger moment needs to be resolved by the sampling density. This constrains the sampling rate to be quite high, therefore the size of the array representing the time-domain waveform will be quite large, slowing down the computation.

The model machine learning gravitational waves from binary neutron stars (`mlgw_bns`) is an attempt to mitigate this problem, by pre-generating Fourier-transformed waveforms.

## 2 Machine Learning

### 2.1 Supervised learning and optimization

Machine Learning is about having an algorithm improve through the use of *training data*, so that is it able to make predictions or decisions automatically, without any specific outcome being explicitly programmed in.

There are many kinds of problems this general approach can be used to solve, the one which is relevant for us here is known as *supervised learning*. The idea is to start from a set of training data consisting of pairs $(x, y)$, where $x$ and $y$ are typically high-dimensional objects, and to train a system so that it is able to reconstruct $y_{\text{new}}$ from a given $x_{\text{new}}$ to within some tolerable margin of error.

Supervised learning differs from *unsupervised* learning, in which data is provided without labels of any sort, and the algorithm must seek some sort of structure in it.

#### 2.1.1 Dataset management

The way a supervised learning system typically works is to build a model $y_{\text{pred}} = f(x; \alpha, \beta)$ which depends on variable parameters $\alpha$ and fixed hyperparameters $\beta$. For concreteness, we can think of polynomial regression: $\beta$ may then be the degree of the polynomial with which we fit the data, while $\alpha$ is the set of coefficients of this polynomial.

We can evaluate the performance of this model by comparing $y_{\text{pred}}$ with the known label $y$ for all the data in the training dataset. This allows us to compute some cost function $C(\alpha; \beta)$ — the choice of $C$ is not simple in general, let us keep it abstract for now.

Then, we can use some optimization procedure to find

$$\bar{\alpha} = \operatorname*{argmax}_{\alpha} C(\alpha; \beta). \tag{2.1}$$

This sounds good, but there is a problem: a procedure as described can get arbitrarily low costs by learning *specific features* of the training dataset which will not generalize. This is known as *overfitting*, and it is characterized by a low error in the training dataset but a high error on new data.

Its counterpart, *underfitting*, may happen when our model is not "detailed" enough to capture some feature of the data. Here, the model will not only perform badly on new data, but also on its training data.

The parameters $\beta$ can typically be adjusted to find an optimum between these two extremes. A concrete example is shown in figure 3: some noisy data is fitted with polynomials of differing degrees — this corresponds to minimizing $C(\alpha; \beta)$ for different values of $\beta$. Only the data in the central region is used for the fit, while the rest is interpreted as validation data.
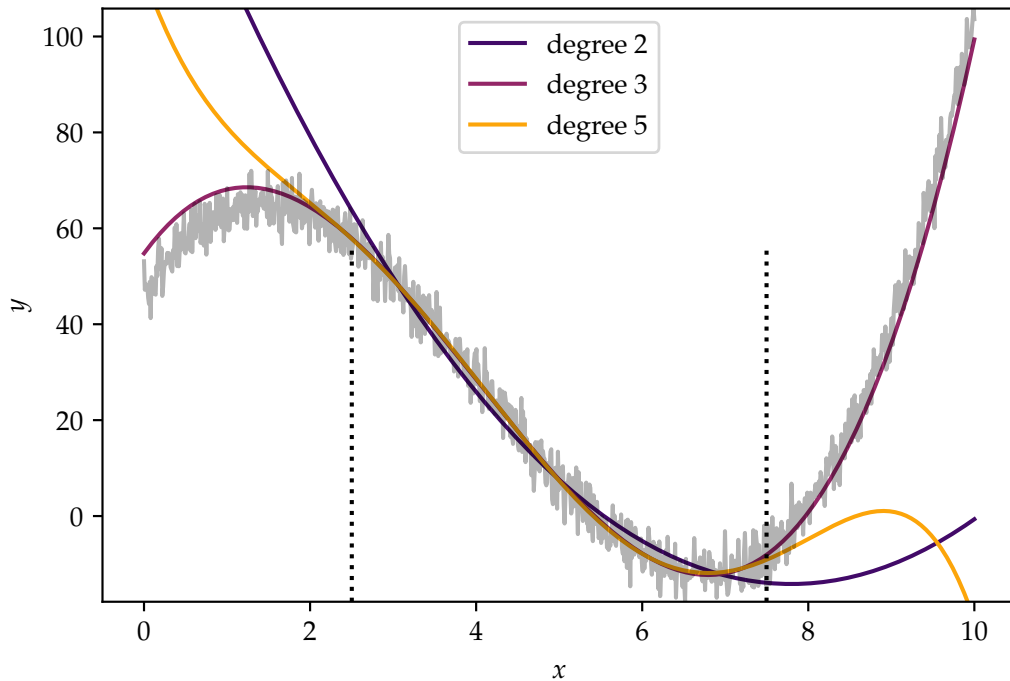


Figure 3: Demonstration of under- and over-fitting: the training data here are the central region between the two vertical lines; the models are then validated in the remaining part of the region. See figure 4 for the exact value of the training and validation errors at various polynomial degrees.

Note that this split of training and validation data, while visually clear, is undesirable in real circumstances: we can achieve much better accuracy if the training data spans every part of the region of interest. This is the case for acmb, since we can generate data at will.

If we denote the error on the validation data as $C_V(\alpha; \beta)$, the full procedure can then be
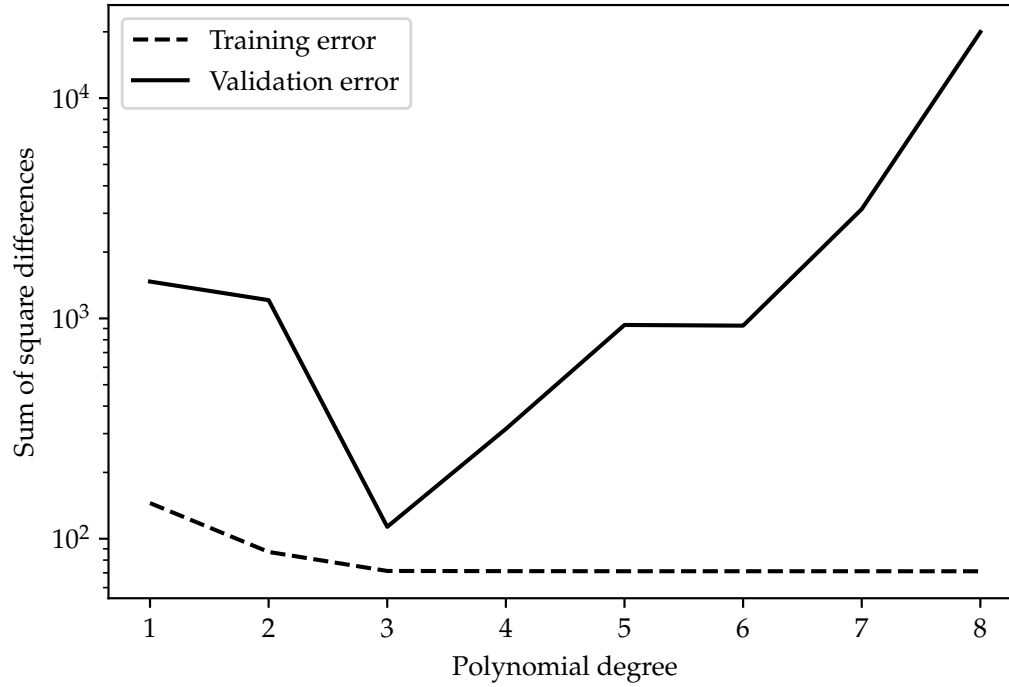
Figure 4: Training and validation errors for figure 3. The best choice for the degree here is clearly 3, since it minimizes the validation error as well as having a very low training error, but without the validation procedure we could not appreciate it being a better choice than higher values.

schematically be written as

$$\overline{\beta} = \underbrace{\operatorname*{argmax}_{\beta}}_{\text{validation}} C_V \left( \underbrace{\operatorname*{argmax}_{\alpha} C(\alpha; \beta); \beta}_{\text{training}} \right). \tag{2.2}$$

The best ways to calculate these two optimums differ, both among each other and on a case-by-case basis: the validation procedure must account for the fact that the training procedure for each value of $\beta$ analyzed can take some time.

In particular, the algorithm used in `mlgw_bns` for training is discussed in section 2.3.4, while the one used for validation is discussed in section 2.4.

The procedure described here makes use of a training and a validation dataset, but typically also we want to have some objective measure of the quality of the fit. This cannot be provided by only using training and validation data information, since the parameters of the model depend on them: we need a third separate *testing* dataset which does not inform

the model in any way.[25]

## 2.2 Principal Component Analysis

After downsampling, a waveform used by `mlgw_bns` is described by several hundred points. It is convenient to reduce this number in order for the neural network to be faster. We are able to do so by making use of the fact that the components of the high-dimensional vector representing the waveform are correlated.

The technique of PCA is quite general,[26] so let us describe it in general terms, and then apply it to our specific problem.

Dimensionality reduction algorithms such as PCA may be considered as a kind of unsupervised learning, since they can allow for the detection of relevant features in high-dimensional datasets. Here we will not use it for this purpose though, it will be more of a pre-processing step.

### 2.2.1 General method

We start with a dataset of $N$ points in $\mathbb{R}^D$, which we denote by $\{x^i\}_{i=0}^{N-1}$. We need $D$ floating point numbers to represent each of these points.

If we can find a $k$-dimensional hyperplane in $\mathbb{R}^D$, with $k \ll D$, such that our points are never very far from this subspace, we can substitute the $D$-dimensional parametrization of the points for a $k$-dimensional one by approximating each point by its orthogonal projection onto the $k$-dimensional hyperplane. We will make a certain error in this process: specifically, if $P_k(x_i)$ denotes the projection of the point onto this hyperplane, the error (computed according to the Euclidean distance among points) can be quantified by

$$\text{error}(k) = \sum_{i=0}^{N-1} \left\| x_i - P_k(x_i) \right\|^2 . \tag{2.3}$$

The algorithm of PCA allows us to determine which hyperplane minimizes this error.

The first step is to center the data: we compute their mean $\overline{x}$, and work with the dataset $y_i = x_i - \overline{x}$. Because of this, we can say that the $k$-dimensional hyperspace is now a *subspace* with respect to $y$. Computationally, we keep the mean $\overline{x}$ saved and add it to the reconstructed data $y$.

Let us now consider the $k = 1$ case: we want to project the data onto a single line, which we can parametrize as the span of a unit vector $w$. Therefore, what we want to minimize is $\sum_i \left\| y_i - (y_i \cdot w)w \right\|^2 = \sum_i \left( \left\| y_i \right\|^2 - (y_i \cdot w)^2 \right)$, and we can do so by maximizing $\sum_i (y_i \cdot w)^2$.

Therefore, the best 1-dimensional subspace is:

$$w = \underset{w \in \mathbb{S}^{D-1}}{\text{argmax}} \sum_i (y_i \cdot w)^2 . \tag{2.4}$$

---

[25] Confusingly, the machine learning (ML) literature sometimes inverts the labels "validation" and "testing" — we shall stick with the definition given above.

[26] This technique is quite old: it was developed in 1901 by Karl Pearson [Pea01; MN17], but it started to see broad use once availability of computers became widespread.

38

Now comes the clever idea of PCA: we can reformulate this argmax problem as an eigenvalue problem for the covariance matrix of the data:

$$C = \frac{1}{N} \sum_i y_i y_i^\top. \tag{2.5}$$

A unit eigenvector $w$ of this matrix will satisfy $Cw = \lambda w$ for its eigenvalue $\lambda$, and we can recover the eigenvalue $\lambda$ from this equation by computing $w^\top Cw = \lambda w^\top w = \lambda$; making the covariance matrix explicit allows us to see that

$$\lambda = w^\top Cw = \frac{1}{N} \sum_i (y_i \cdot w)^2 \,; \tag{2.6}$$

which is precisely the quantity we wanted to maximize: therefore, the best one-dimensional subspace is precisely the largest eigenvector of the covariance matrix, the direction of maximum variance.

If we make the further observation that the covariance matrix is symmetric and positive definite, and can therefore be orthogonally diagonalized, we are almost done: we can generalize to arbitrary $k$ moving one vector at a time. To find the second vector to span the subspace we can restrict ourselves to the subspace $w^\perp$ and apply the same procedure as before, this tells us that the optimal two-dimensional subspace is the span of the first two eigenvectors of the covariance matrix, and so on.

In order to perform a reduction onto a $k$-dimensional subspace, then, we need to calculate the unit eigenvectors $\{w_i\}_{i=0}^{k-1}$ corresponding to the $k$ largest eigenvalues; we can understand these as the columns of a $D \times k$ matrix $V$, which we can then use to construct the projection matrix onto the $k$-dimensional subspace.

In terms of the $D$-dimensional coordinates, the projection matrix is $VV^\top$: its application to a vector $y$ can be written as

$$P_k(y) = VV^\top y = \begin{bmatrix} w_1 & \cdots & w_k \end{bmatrix} \begin{bmatrix} w_1 \\ \vdots \\ w_k \end{bmatrix} y = \sum_{i=0}^{k-1} (w_i \cdot y) w_i \in \mathbb{R}^D. \tag{2.7}$$

For the purpose of dimensionality reduction, however, we are not interested in this projection, which still yields a $D$-dimensional vector: all the "reduced" vectors lie in a $k$-dimensional subspace, therefore we express them with only $k$ coordinates, by computing $V^\top y \in \mathbb{R}^k$.

If we approach the problem by diagonalizing the covariance matrix $C$, the computational complexity in the worst case scenario is $\mathcal{O}\left(D^3\right)$, since it involves the diagonalization of a $D \times D$ matrix.

### 2.2.2 PCA for waveforms

After downsampling and computing the residuals from the PN waveform, we are left with a waveform described by a vector of a few hundred points for the amplitude and similarly for the phase.

It would be possible to perform PCA separately for these two vectors; however if we combine them into a single one we can exploit any existing correlation between the amplitude and phase residuals. In the worst case scenario — amplitude and phase residuals being completely uncorrelated — this procedure will perform exactly like separating the PCA into two. So, we want to combine amplitude and phase residuals into a single vector.

A simple way to do so is to simply "append" one vector to the other, and therefore consider the waveform as a vector in $\mathbb{R}^{D_A+D_\varphi}$. There is an issue with this procedure: PCA optimizes Euclidean distance, so the scaling of the amplitude and phase residuals becomes relevant. Fortunately, this carries no physical meaning: because of the way we define the residuals 3.2.1, it is equivalent to a change in the basis for the logarithm.

Heuristically, we want the typical scale of the phase residuals to roughly match that of the amplitude residuals. This can be simply achieved by multiplying either part of the vector by a constant, which can be tuned in order to optimize the reconstruction error.
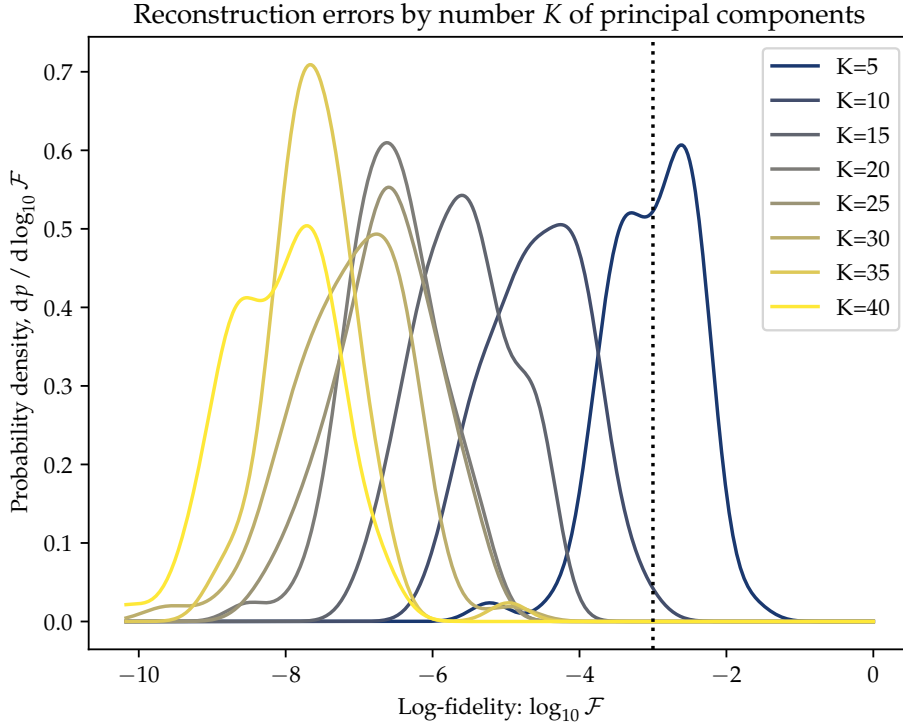


Figure 5: The reconstruction error is computed after projecting onto a $K$-dimensional subspace a number $N_w = 64$ waveforms. The parameters for the PCA model are fitted with an independent, $N_{\mathrm{PCA}} = 128$ waveform dataset. A KDE is performed for each set of corresponding log-fidelities, in order for the probability curve to look smoother. Here the EOB waveforms are calculated with a SPA. A vertical dashed line indicates a "desirable" maximal reconstruction error, $\mathcal{F} \sim 10^{-3}$, which roughly corresponds to the accuracy of the underlying EOB model to NR simulations.

## 2.3 Neural Networks

After the reduction of dimensionality through PCA, we are left with the task of approximating the map between the parameters of the system generating the waveform, $\theta_i$, and the $k$ principal components.

In the work of Schmidt et al. [Sch+20] this was accomplished through a Mixture of Experts model, which amounts to a fit to a polynomial expression of the parameters; here instead we reconstruct the function with a neural network.

NNs are known to be able to approximate arbitrary functions [Nie15], and in practice they are quite versatile and usually not prone to overfitting. In the next section we will describe the architecture of a multi-layer perceptron regressor, the kind of network used by `mlgw_bns`.

### 2.3.1 Multi-layer perceptrons

This architecture is built in order to solve the problem of reconstructing a map from an input $x_i \in \mathbb{R}^n$, to an output $y_i \in \mathbb{R}^k$.

We introduce a *hidden layer* between the input and the output. This consists of a certain number $m$ of "neurons", which can be more or less activated as a function of the inputs. Specifically, the $j$-th neuron in the hidden layer will have an activation level given by the expression:

$$z_j = \sigma\left(w_{ji}^{(1)} x_i + b_j^{(1)}\right), \tag{2.8}$$

where $\sigma\colon \mathbb{R} \to \mathbb{R}$ is called the *activation function*, while the parameters $w_{ji}^{(1)}$ and $b_j^{(1)}$ are respectively called the *weights* and the *biases* (for the first hidden layer).

We shall discuss the reasons one might have for choosing different activation functions later; for now let us say that it is typically differentiable almost everywhere, and it achieves low values for low inputs and high values for high inputs. A common choice, for example, is a logistic sigmoid in the form $\sigma(z) = (1 + e^{-z})^{-1}$.

The weights and biases of the network are free parameters, real numbers which will need to be tuned by the training process.

Once the network has computed the activations $z_j$ for our single hidden layer, it can compute the activations for the output: in this last stage we use no activation function, and the output of the network is simply

$$y_\ell = w_{\ell j}^{(2)} z_j + b_\ell^{(2)} = w_{\ell j}^{(2)} \sigma\left(w_{ji}^{(1)} x_i + b_j^{(1)}\right) + b_\ell^{(2)}. \tag{2.9}$$

In the end, therefore, the number of free parameters of the network is $nm + m$ for the first layer and $mk + k$ for the second, so $m + k + m(n + k)$ in total.

Adding more layers is not conceptually different, it only amounts to applying the procedure described by equation 2.8 again to the result of the first layer, and so on; each time we use the activation function, except for the output layer.

The activation function is crucial for our network to be able to capture nonlinearities: if we were to remove it, with any number of layers the network would still be a linear function of the inputs.

The implementation we use for `mlgw_bns` is the one provided by `scikit-learn` [Ped+11]; specifically, we choose an `MLPRegressor`.[27]

### 2.3.2 Training

The network is able to reconstruct our function as long as the weights and biases are appropriately set: how do we train it to ensure this?

We need to assign a loss function to the output of the network. Here, simplicity trumps accuracy — the "true" error we might like to work with is given by the Wiener distance among waveforms reconstructed from their PCA components, but in order to efficiently train the network we need something easier to compute. The typical error chosen is quadratic in the Euclidean distance, since its analytical derivative is easy to compute:

$$\text{error}(y) \propto \sum_{\text{training data}} \left\| y_{\text{predicted}} - y_{\text{true}} \right\|^2. \tag{2.10}$$

We also add an error term in the form $\alpha \|W\|^2$, where $\alpha$ is a non-negative hyperparameter (typically chosen to be small) and $\|W\|^2$ is the L2 norm of the weight tensor: this term is known as a "regularizer", it penalizes complex models. The reason why the L2 norm specifically is often chosen is because of the simplicity and efficiency of its implementation.[28] The parameter $\alpha$ is optimized in the hyperparameter training procedure.

We are then using the Euclidean distance among the $y$s (which for us will be PCA component vectors) as a measure of the performance of the network; this works well enough, but we can make an improvement by noticing that the first PCA components are responsible for more of the variance (and thus more of the distance) between data points. Therefore, we can improve the performance by having the network learn the distance among the rescaled

$$\text{PC}_i \lambda_i^\kappa, \tag{2.11}$$

where $\lambda_i$ are the eigenvalues corresponding to the principal components, while $\kappa > 0$ is a hyperparameter. The prior distribution for $\kappa$ is a log-uniform one between $10^{-3}$ and 1.

### 2.3.3 Backpropagation

Once we have our cost function, we need a rule to change the weights $w_{ij}^l$ and biases $b_j^l$ of our network[29] according to the variation of the cost function. We would like to implement some sort of gradient descent algorithm, updating weights and biases by

$$\Delta w_{ij}^l = -\eta \frac{\partial C}{\partial w_{ij}^l} \qquad \text{and} \qquad \Delta b_j^l = -\eta \frac{\partial C}{\partial b_j^l}, \tag{2.12}$$

---

[27] The documentation for this network can be found at the url https://scikit-learn.org/stable/modules/generated/sklearn.neural_network.MLPRegressor.html.

[28] In the backpropagation equations, which we will shortly introduce, this eventually translates to a penalty on the update of each weight proportional to the weight itself. The overhead needed in order to compute this is very small.

[29] We have added an index $l$ for the layer: so, $w_{ij}^l$ is the weight that the $j$-th neuron in the $l$-th layer gives to input $i$.

where $\eta$ is called the *learning rate*.

So, we need to compute the gradients $\partial C / \partial w_{ij}^l$ and $\partial C / \partial b_j^l$. The first idea one might have to do so is to approximate them to first order, doing something like

$$\frac{\partial C}{\partial w_{ij}^l} \approx \frac{C(w + \epsilon e_{ij}^l) - C(w)}{\epsilon}, \tag{2.13}$$

where $w$ is the full weight tensor, while $\epsilon e_{ij}^l$ represents a small increment to that particular weight, $e$ being a "unit tensor".

This strategy turns out to be unfeasible because of its computational complexity: the computation of the cost requires a full pass-through of the network, requiring at least $M$ floating point operations (additions or multiplications) where $M$ is the number of free parameters. This would need to be done to compute the update of each of these parameters, so the number of operations needed to perform a single step of the gradient descent for the full network would be at least $M^2$.

The backpropagation algorithm is a clever idea which allows us to compute the gradient with only a forward pass through the network followed by a backward pass, exploiting the chain rule and the way the weight matrices affect each other iteratively.

The algorithm can be summarized by the following equations [Nie15, chapter 2]:

$$\frac{\partial C}{\partial w_{jk}^l} = a_k^{l-1} \delta_j^l \tag{2.14}$$

$$\frac{\partial C}{\partial b_j^l} = \delta_j^l \tag{2.15}$$

$$\delta_j^l = \left( \sum_i w_{ij}^{l+1} \delta_i^{l+1} \right) \sigma'(z_j^l) \tag{2.16}$$

$$\delta_j^L = \frac{\partial C}{\partial a_j^L}, \tag{2.17}$$

where $a_j^l = w_{ji}^l z_i + b_j^l$ is the activation for the $j$-th neuron of layer $l$, while $z_j^l = \sigma(a_j^l)$ is the output of the activation function for $a_j^l$.

It is important to note that the backpropagation equations are written without the Einstein summation convention: "$x_j = y_j z_j$" means that the $j$-th component of the vector $x$ is calculated by multiplying the $j$-th components of the vectors $y$ and $z$. This means that we are not computing matrix products, but instead the element-wise Hadamard product.

Working backwards, the last equation tells us how to compute the error corresponding to the output layer, denoted with $L$. We can compute the derivative of the cost function with respect to the activation analytically if, for example, we are using a simple quadratic cost function as described in equation 2.10.[30]

The second-to-last equation tells us how to compute the error $\delta_j^l$ of a layer if we know the error of the following layer. It is an application of the chain rule. We compute the $\delta_j^l$

---

[30] The expression in [Nie15] differs from this one since he applies the activation function to the last layer, which one should do for a classification algorithm but not for a regression algorithm.

iteratively going backwards through the network, and having done so we can recover the derivative of the cost with respect to the weights and biases by combining the error $\delta_j^l$ with the activations of each layer, $a_k^{l-1}$, as described by the first two equations.

### 2.3.4 Stochastic gradient descent

The method for gradient descent described by equation 2.12 is still slow if we try to compute the gradient of the cost function by using all the training data we have. It turns out to be more efficient to compute the gradient by only looking at a single example or a small batch of them, chosen randomly: this idea is known as *stochastic gradient descent*.

This typically allows for much faster convergence of the training process.

The algorithm used for the training of the network in `mlgw_bns` is Adam [KB17; Rud16], short for "Adaptive Moment Estimation", as implemented in `scikit-learn` [Ped+11].

The general idea of this algorithm is, first, to not move directly in the direction of the gradient, but instead to keep a running, exponentially weighted average of it, and move in *that* direction. An example where we can imagine this could be useful is if the cost function landscape exhibits a "canyon", with a low slope in a long and narrow central region and steep walls. A direct move in the direction of the gradient might mean we "bounce" between the walls a lot without being able to settle in the middle, while averaging allows the direction of our movement to be smoothed and perhaps fall in the middle region.

The second aspect is to make the step-size adaptive, as opposed to it being strictly proportional to the gradient. A "signal-to-noise ratio" is estimated through the square of the gradient, and it is used to scale the step based on how confident we might be in it being meaningful or not.

Both of these exponential decays are regulated by a hyperparameter — $\beta_1$ and $\beta_2$ respectively, which are commonly set to $\beta_1 = 0.9$ and $\beta_2 = 0.999$, but which can be optimized.

## 2.4 Hyperparameter optimization

Our network will depend on several hyperparameters, such as the number and size of the layers or the learning rate; we want to get as close as possible to the optimal choice of these for the reconstruction of the function mapping the binary system parameters to the principal components to be fast as well as accurate.

This optimization is accomplished through a multi-objective tree-structured Parzen estimator (MOTPE), as described in Ozaki et al. [Oza+20] and as implemented through the Optuna API [Aki+19].

Here we will summarize the mechanism through which a single objective tree-structured Parzen estimator (TPE) works, as originally described in Bergstra et al. [Ber+11, section 4], since the generalization to the multi-objective case [Oza+20] is rather mathematically involved but not too conceptually dissimilar from the single-objective case.

We can abstract away the neural network as a function $f$ which, after being given a set of hyperparameters $\vec{x}$, outputs a cost $y$, which we want to minimize. The evaluation of $f$ is quite costly: it involves the training of the network and a full evaluation of its performance

(in our case, the reconstruction of the waveforms and a computation of the Wiener distance to their true counterparts).

So, we want to find a value of $\vec{x}$ which minimizes $y$ with as few evaluations of $f$ as possible. The parameters $\vec{x}$ will be given certain prior distributions initially, from which their values will be drawn randomly. Let us then suppose we already have a set of observations $\{(\vec{x}_i, y_i)\}_i$, and we want to find the best possible new value of $\vec{x}$.

We choose a certain quantile $\gamma$, say 15%, and select a fraction $\gamma$ of the best observations we have. This allows us to find a $y^*$ such that $\mathbb{P}(y < y^*) = \gamma$.

Then, we approximate the probability density $p(\vec{x}|y)$ as follows:

$$p(\vec{x}|y) = \begin{cases} \ell(\vec{x}) & y < y^* \\ g(\vec{x}) & y \geq y^*. \end{cases} \tag{2.18}$$

We are condensing the $y$-dependence onto a binary choice between "good" observations, modelled by $\ell(\vec{x})$, and "bad" observations, modelled by $g(\vec{x})$. These two functions can then be estimated by making use of the observations we have in the $y < y^*$ and $y \geq y^*$ cases.

This, crucially, allows us to calculate the **expected improvement** associated with a certain parameter set $\vec{x}$:

$$\text{EI}_{y^*}(\vec{x}) = \int_{-\infty}^{\infty} \max\left(y^* - y, 0\right) p(y|\vec{x})\, \mathrm{d}y \tag{2.19}$$

There is no improvement if $y > y^*$.

$$= \int_{-\infty}^{y^*} (y^* - y) p(y|\vec{x})\, \mathrm{d}y \tag{2.20}$$

$$= \int_{-\infty}^{y^*} (y^* - y) \underbrace{p(\vec{x}|y)}_{=\ell(\vec{x})} p(y) \frac{1}{p(\vec{x})}\, \mathrm{d}y \tag{2.21}$$

Used $p(x,y) = p(x|y)p(y) = p(y|x)p(x)$.

$$= \frac{\ell(\vec{x})}{\gamma \ell(\vec{x}) + (1-\gamma)g(\vec{x})} \underbrace{\int_{-\infty}^{y^*} (y^* - y) p(y)\, \mathrm{d}y}_{\text{independent of } \vec{x}} \tag{2.22}$$

Expanded $p(\vec{x})$ as $\int p(x|y)p(y)\,\mathrm{d}y$ and split the $\ell$ and $g$ cases.

$$\propto \frac{1}{\gamma + (1-\gamma)\frac{g(\vec{x})}{\ell(\vec{x})}}, \tag{2.23}$$

where the term we neglected can be interpreted as the average improvement over all choices of $\vec{x}$, which we hope is large but which we cannot affect with a good choice of $\vec{x}$.

What this tells us is the rather intuitive fact that we want to select points which are favored by the "good" distribution $\ell$ and not by the "bad" distribution $g$, so that $g/\ell$ is small, which means that the expected improvement will be large. The formula also says that we should prefer smaller values of $\gamma$, but it does not take into account the fact that we need a reasonably large selection of points in order to properly model $\ell(\vec{x})$ without a large error. The balance among these two contrasting desires will dictate our choice of $\gamma$.

Once we are able to compute the expected improvement, the task is simple: we just need to generate a selection of points $\vec{x}_i$ from the distribution $\ell(\vec{x})$, evaluate their expected improvement (or just $g/\ell$, really) and pick the one with the largest expected improvement as the one for which to evaluate the neural network (NN).

The one aspect still missing in the algorithm is how to estimate a probability distribution from a small set of samples, and how to calculate a new sample from it. There are different ways to do so; the one implemented in the TPE algorithm fits a gaussian mixture model to estimate $\ell(\vec{x})$ and $g(\vec{x})$ [BYC13, section 5].

## 3 MLGW-BNS

Let us start with an overview of the algorithm employed by `mlgw_bns` before getting into the technical details.

We start with two systems for the generation of a theoretical waveform from a CBC in the frequency domain, one being faster but less accurate than the other. The "fast" system will be the PN model `TaylorF2`, as implemented in `bajes` [BGB21], while the "slow" system will be the EOB model `TEOBResumS`, with waveforms generated in the time domain and then Fourier-transformed.

As we shall see shortly, a crucial feature of the "fast" system is the capability to generate waveforms in the frequency domain at select frequencies, without needing to perform a full Fourier transform from a time-domain waveform. This feature is shared by all PN approximants, which base their Fourier-domain representations on the analytic SPA.

The main idea is then to

1. compute the residuals of the "slow" waveforms from the "fast" ones, and with these build a dataset;

2. train a machine learning system on this dataset, so that it is able to reconstruct the map from the parameters $\vec{\theta}$ to the residuals.

If this task is accomplished with tolerable errors and with a fast enough execution time (shorter than the time taken by the "slow" generation method) we will have a working *surrogate model*.

The generation of datasets needs us to define a probability distribution over the parameter space: the density of points in each region will bias the reconstruction, but this might actually be desirable if we need to sample from certain regions more than others. A good choice, therefore, could be to generate the training dataset according to a prior distribution over the parameters.

The implementation currently active in `mlgw_bns`, however, simply generates waveforms with a uniform distribution over the selected parameter ranges: $q \in [1, 2]$, $\Lambda_i \in [5, 5000]$[31] and $\chi_i \in [-0.5, 0.5]$.

The nonspinning case, which will be discussed later, simply amounts to restricting the prior to the three-dimensional subspace, such as $\chi_i \equiv 0$.

---

[31] The reason why $\Lambda \to 0$ is not included in the range is that the EOB model used is unstable very small $\Lambda$, since certain computations include divisions by it.

## 3.1 Training waveform generation

The output of the EOB and PN we use is able to output both $h_+$ and $h_\times$, but this is redundant for our purposes: the ratio between them is a $\pi/2$ phase combined with a factor depending on the inclination angle $\iota$: the two polarizations can be expressed as $h_+(f) = h_0(f)(1+\cos^2\iota)/2$ and $h_\times(f) = h_0(f)(-i)\cos\iota$. The "base" waveform $h_0(f)$ can therefore be interpreted as the plus-polarized waveform in the $\iota = 0$ case.

If we reconstruct it, we can recover $h_+$ and $h_\times$ for arbitrary inclination using the two aforementioned expressions.

Also, we work in natural units: we treat the waveform as a function of $Mf$, which is dimensionless if $G = c = 1$. We must be careful, however, since while the time-domain strain $h(t)$ is dimensionless its Fourier transform $\widetilde{h}(f)$ has the dimensions of a time, or a mass.

Let us rewrite the SPA, 0PN expression for the amplitude (the absolute value of equation A.18 for $\iota = 0$) to illustrate this point:

$$\frac{\widetilde{h}_+(f)}{M} = \frac{1}{\pi^{2/3}}\sqrt{\frac{5}{24}}(Mf)^{-7/6}\frac{M}{r}\sqrt{\nu}, \tag{3.1}$$

where we use natural units, as well as employing the relation $\mathcal{M}_c = M\nu^{3/5}$ 1.68.

## 3.2 Phase unwrapping

The waveforms generated by the EOB system are complex-valued, in the form $h_(f) = A(f)e^{i\phi(f)}$.

It is useful for the later stages of this algorithm to decompose such a waveform into $A(f)$ and $\phi(f)$, however in doing one runs into a complication. The amplitude can be simply calculated as $A(f) = |h(f)|$, but the phase computed as $\angle h(f)$ is bounded (between $-\pi$ and $\pi$ in the numpy implementation), therefore it is discontinuous when $h(f)$ crosses the negative real axis.

In order to overcome this issue we need to make some assumptions about the waveform: we ask that the phase $\phi(f)$ is smoothly varying, densely sampled and almost monotonic.

The first two conditions, in practice, refer to the fact that the variation of the phase between two sample points should be small compared to $2\pi$ — otherwise, we would not be able to tell whether it increased by $x$ or $2\pi n + x$ for some integer $n$.

If $\phi(f)$ were very densely sampled, such that $\Delta\phi$ between two successive points were always $< \pi$, we could drop the condition of almost-monotonicity: an algorithm could simply compute $\angle h(f)$ for each sample point, and add $2\pi n$ as needed in order to make the differences between successive points $< \pi$. This is the algorithm implemented, for example, by the unwrap function in the numpy library [Har+20].

We can do slightly better, however, by using the quasi-monotonicity assumption and treating decreasing phase differently than increasing phase: we add $2\pi n$ to each point, determining $n$ so that $\phi_{i+1} - \phi_i \in [-\epsilon, 2\pi - \epsilon]$, where $\epsilon$ is some small number quantifying the maximum decrease in phase we expect to see. If $\epsilon = \pi$ this is equivalent to the numpy algorithm.

The monotonicity and magnitude of the phase are not invariant: we can add a general linear term $2\pi f t_0 + \phi_0$ to $\phi$ by changing the initial phase and the coalescence time. However, within the convention we are using (where the coalescence happens at the edge of the sample range) the phase of $h(f)$ is indeed almost monotonic, such that $\epsilon \sim 10^{-1}$ is typically a good choice.

Since this implementation is custom-made it is also slightly faster: it takes $\sim 30\,\text{ms}$ to unwrap a waveform with $\sim 5 \times 10^5$ sampling points, as opposed to the $\sim 40\,\text{ms}$ needed for the `numpy` implementation.

### 3.2.1 Residual calculation
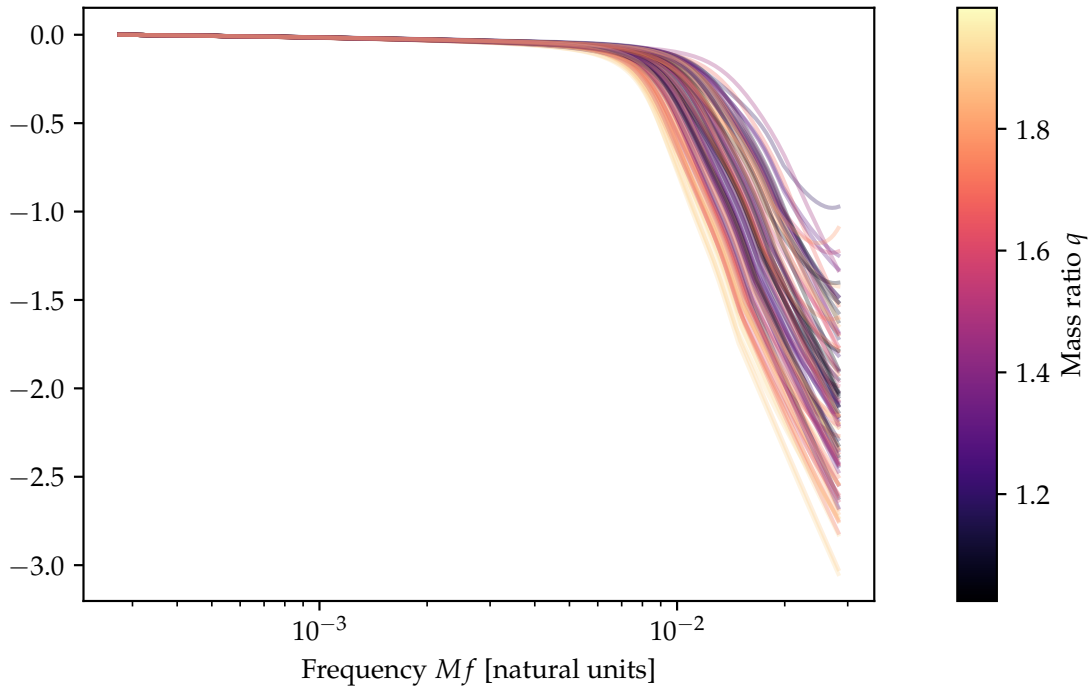


Figure 6: Residuals in amplitude of the EOB waveforms versus the PN ones. The waveforms are uniformly distributed across all five parameters.

The computation of the residuals is made easier by the fact that we have closed-form expressions for the PN waveforms to high order, including tidal effects.

Using higher-order waveforms means that the residuals to fit are smaller, but this comes with a large drawback: the evaluation time of the
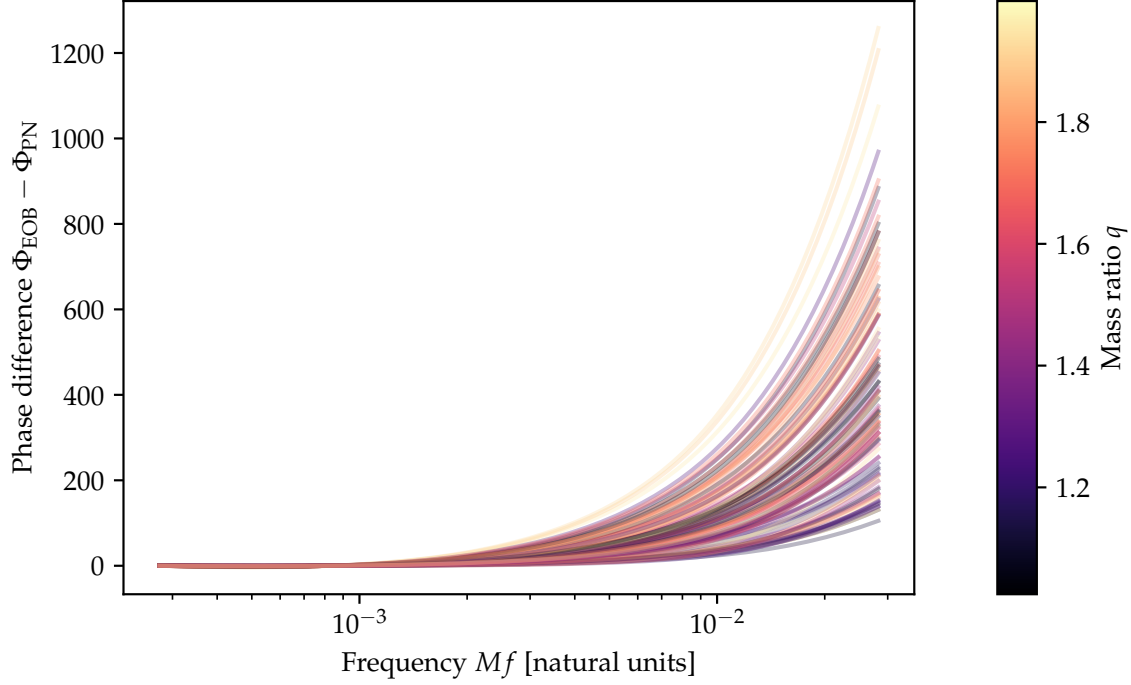
Figure 7: Residuals in phase of the EOB waveforms versus the PN ones. The waveforms are uniformly distributed across all five parameters.

### 3.2.2 Greedy downsampling

The residual waveforms generated with the EOB / PN models have on the order of a few times $10^5$ sampling points. This is too large a number to effectively use PCA on: as we will see, it requires writing a covariance matrix which would have $\sim 10^{11}$ entries, way beyond the RAM of most computers.

Therefore, we need to start by applying a simple dimensionality reduction technique: downsampling, applied to the unwrapped phase and amplitude of waveforms (see section 3.2) after the subtraction of the "baseline" PN ones.

Doing so on a uniform grid, however, is suboptimal: there is more detail to be captured in some areas than in others. It is difficult to determine *a priori* which areas will be more relevant than others, therefore `mlgw_bns` implements a greedy algorithm which selects a set of indices which optimize the reconstruction accuracy, inspired by `romspline`, which was introduced by Galley and Schmidt [GS16].

The algorithm is detailed as algorithm 2; it includes certain improvements over `romspline`. First, it allows for a full training dataset as opposed to reconstruction of a single waveform. The points are greedily chosen until the error over the whole dataset is below the threshold. This allows us to be more confident of the fact that the indices are not capturing the specifics of a single waveform, but instead they are representative of the whole dataset.

Whether this is actually happening

The interpolation method to choose is also important: higher-order interpolants are slower but need less points. Here we use cubic splines, which have been found to be a good compromise for surrogate models [Lac+19].

---

**Algorithm 2** Greedy downsampling algorithm.

---

**Require:** $x_i$, $y_i^{(j)}$, tolerance $\epsilon$.
**Require:** "Seed" indices $I$
  Error $e \leftarrow 0$
  **while** $e > \epsilon$ **do**
    $e \leftarrow \infty$
    **for** each $j$ **do**
      $I' \leftarrow \varnothing$
      $e_j \leftarrow 0$
      $y_{\text{rec},i}^{(j)} \leftarrow$ interpolation of $x_I$, $y_I^{(j)}$
      **for** $k_1, k_2$ successive pair in $I$ **do**
        $n \leftarrow \text{argmax}_{i \in [k_1,k_2]} \left| y_{\text{rec},i}^{(j)} - y_i^{(j)} \right|$
        $e_j \leftarrow \max \left( e_j, \left| y_{\text{rec},n}^{(j)} - y_n^{(j)} \right| \right)$
        **if** $\left| y_{\text{rec},n} - y_n^{(j)} \right| > \epsilon$ **then**
          $I' \leftarrow I' \cup n$
        **end if**
        $I \leftarrow I \cup I'$
      **end for**
      $e \leftarrow \min(e, e_j)$
    **end for**
  **end while**
  **return** indices $I$

---

## 3.3 The reconstruction of a waveform

# A The Stationary Phase Approximation

We can apply SPA to approximate the Fourier transform of an oscillatory function $f(t) = A(t)e^{-i\Phi(t)}$ as long as [CF98]

1. $\dot{\Phi}$ is monotonic;

2. the amplitude $A(t)$ is slowly changing compared to the phase: $\left| \dot{A}/A \right| \ll \left| \dot{\Phi} \right|$;

3. the phase derivative is slowly varying: $\left| \ddot{\Phi} \right| \ll \dot{\Phi}^2$.
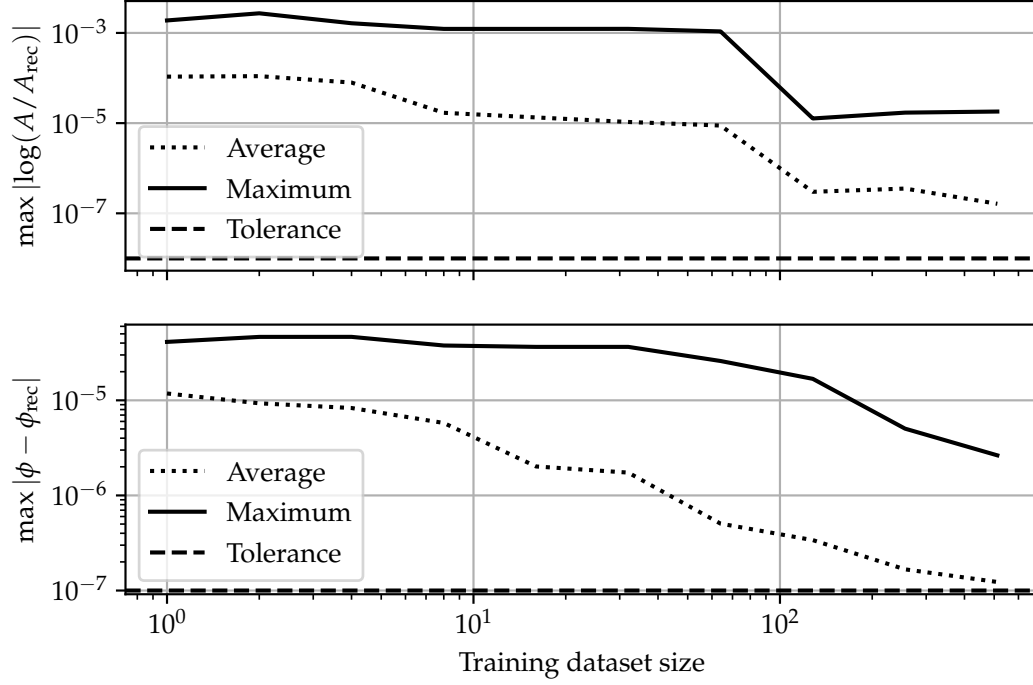
Figure 8: Validation errors for downsampled waveforms. Downsampling indices are calculated by applying algorithm 2 to a dataset of varying size, and the error is calculated by computing the maximum reconstruction error for each of $N_{\text{val}} = 128$ waveforms. Note that "average" and "maximum" here refer to the difference between taking an average or a maximum over the array of maximum reconstruction errors.

If these conditions hold, then in the computation of the transform

$$\widetilde{f}(\omega) = \int_{-\infty}^{\infty} \mathrm{d}t\, A(t) e^{-i\Phi(t)+i\omega t} \tag{A.1}$$

the exponential term will be quickly oscillating, and therefore destructively interfering, almost everywhere; while near the time in which $\omega = \dot{\Phi}$ it will have a positive contribution.

With this in mind, we can approximate the integral: specifically, looking at the local integral contribution to the integral in figure 10 we can see that it approaches a Gaussian,[32] which suggests expanding the argument of the exponential to second order around its stationary point,

$$-i\Phi(t) + i\omega t \approx \left(-i\Phi(t) + i\omega t\right)\Big|_{t_s} - \frac{i}{2}\left.\ddot{\Phi}\right|_{t_s}(t - t_s)^2, \tag{A.2}$$

---

[32] The noise is mostly due to the window choice — a rectangular window is clearest for the visualization, but smoother choices yield less noise.
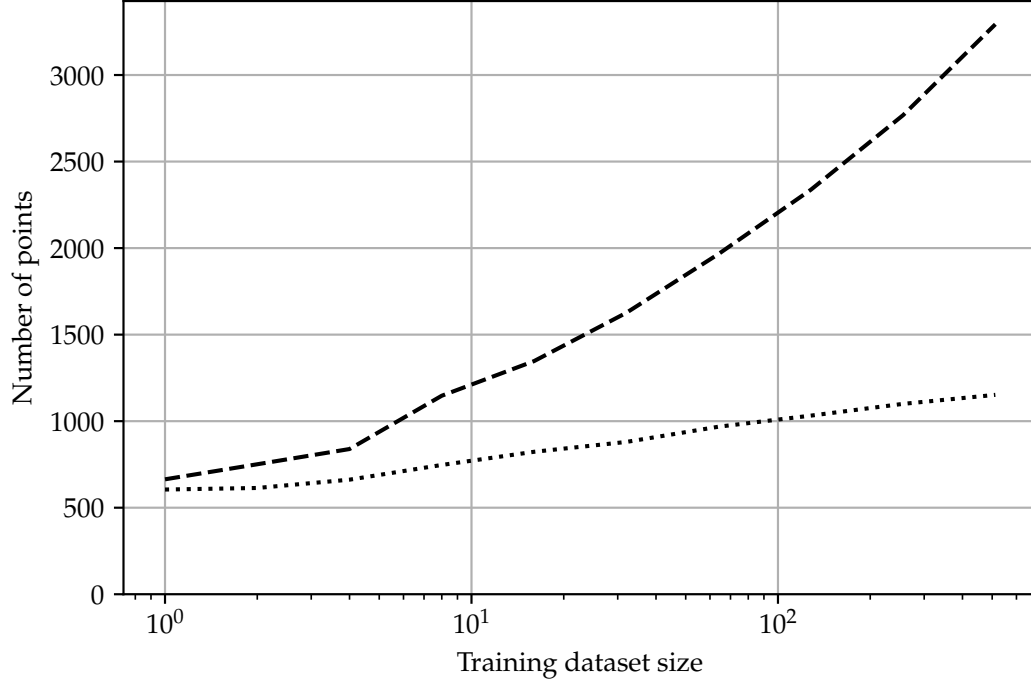
Figure 9: Size of the downsampling index array deriving from the application of algorithm 2 to datasets of varying sizes.

where the stationary time $t_s$ is precisely the one such that $\dot{\Phi}(t_s) = \omega$ (which means that the linear term of the expansion vanishes).

The Fourier integral then looks like

$$\widetilde{f}(\omega) \approx \int_{-\infty}^{\infty} dt\, A(t) \exp\left(-i\Phi(t_s) + i\omega t_s\right) \exp\left(-\frac{i}{2}\ddot{\Phi}(t - t_s)^2\right), \qquad (A.3)$$

so the $t$-dependent part of the integral looks like the product of the amplitude and a "complex Gaussian". There is an analytic formula for a complex Gaussian integral

$$\int e^{i\alpha x^2}\, dx = \sqrt{\frac{\pi i}{\alpha}}, \qquad (A.4)$$

however, in order to apply it, we need to approximate the amplitude as constant: $A(t) \approx A(t_s)$. This will be valid as long as the variation of the amplitude is small in the width of the Gaussian we are integrating it against, which is $\sigma = 1/\sqrt{\ddot{\Phi}}$, so a condition we might write is $(\dot{A}/A)(1/\sqrt{|\ddot{\Phi}|}) \ll 1$. Notice that the combination of the conditions we imposed at the beginning ensures this.
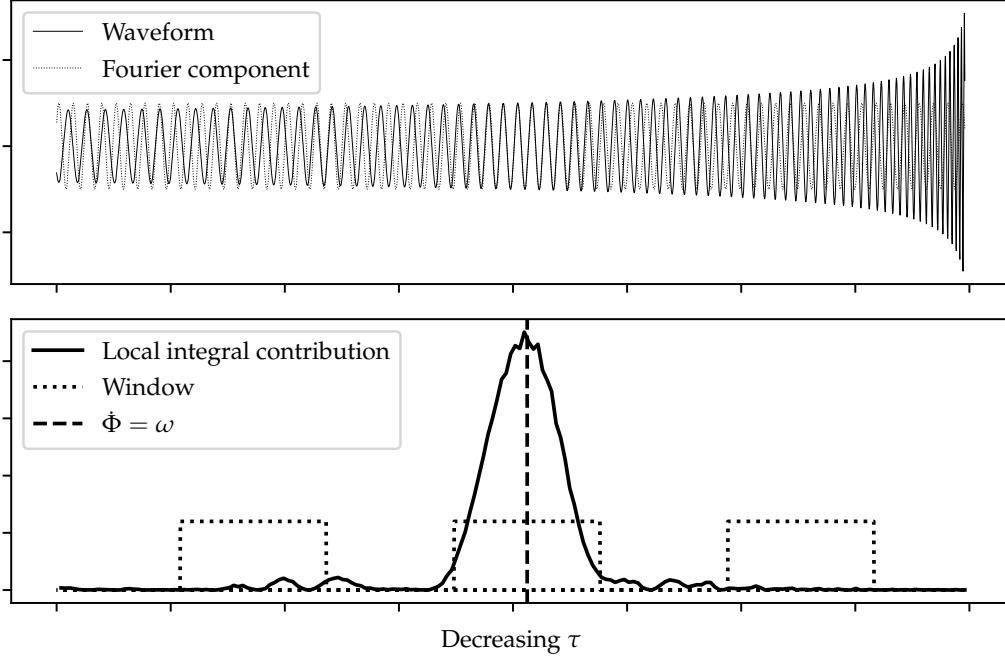
Figure 10: Visualization of the idea behind SPA. In the upper plot we show a typical waveform for a CBC together with a sinusoid corresponding to the ones used in the computation of the Fourier transform. The lower plot shows a windowed Fourier-like integral, in the form $I(t_0) = \int h(t)\cos(\omega t)w(t - t_0)\,dt$ for some window function $w$ centered on $t - t_0 = 0$, as well as three copies of the window. The value plotted with a solid line is $|I(t_0)|^2$. It can be clearly seen that in the regions where there is a frequency mismatch the contribution vanishes.

If this is the case, we can write the Fourier integral as

$$\widetilde{f}(\omega) \approx A(t_s)e^{-i\Phi(t_s)+i\omega t_s}\sqrt{\frac{-2\pi i}{\ddot{\Phi}}} \tag{A.5}$$

$$\left|\widetilde{f}(\omega)\right| \approx A(t_s(\omega))\sqrt{\frac{2\pi}{\ddot{\Phi}(t_s(\omega))}} \tag{A.6}$$

$$\angle\widetilde{f}(\omega) \approx -\Phi(t_s(\omega)) + \omega t_s(\omega) - \frac{\pi}{4}\,, \tag{A.7}$$

where the $-\pi/4$ comes from the $\sqrt{-i}$.

We want to apply this to the specific case of $A$ and $\Phi$ being given by polynomial expressions like the formulas describing quadrupole emission: (1.75) and (1.73); for simplicity, let us write these as

$$\Phi(t) = K_\Phi(-t)^\alpha \quad \text{and} \quad A(t) = K_A(-t)^\beta\,, \tag{A.8}$$

where the reason for writing $(-t)$ is that the aforementioned equations are written in terms of the time until merger $\tau$ — $t = -\tau$ is increasing and equal to 0 at the merger. We do not

specify the polarization, the argument will apply for both. The true values for the exponents in the quadrupole approximation are $\alpha = 5/8$ and $\beta = -1/4$.

The first thing to do is to find $t_s(\omega)$: it is given by

$$\omega = \dot{\Phi} = \alpha K_\Phi (-t_s)^{\alpha-1} \tag{A.9}$$

$$t_S = -\left(\frac{\omega}{\alpha K_\Phi}\right)^{1/(\alpha-1)}. \tag{A.10}$$

The other quantities we need to compute are:

$$A(t_s) = K_A \left(\frac{\omega}{\alpha K_\Phi}\right)^{\beta/(\alpha-1)} \tag{A.11}$$

$$\Phi(t_s) = K_\Phi \left(\frac{\omega}{\alpha K_\Phi}\right)^{\alpha/(\alpha-1)} \tag{A.12}$$

$$\ddot{\Phi}(t_s) = K_\Phi \alpha(\alpha-1)(-t_s)^{\alpha-2} = -K_\Phi \alpha(\alpha-1)\left(\frac{\omega}{\alpha K_\Phi}\right)^{(\alpha-2)/(\alpha-1)}, \tag{A.13}$$

therefore the phase reads

$$\angle \tilde{f}(\omega) = -K_\Phi \left(\frac{\omega}{\alpha K_\Phi}\right)^{\alpha/(\alpha-1)} - \omega \left(\frac{\omega}{\alpha K_\Phi}\right)^{1/\alpha} - \frac{\pi}{4} \tag{A.14}$$

$$= -\left(\frac{\omega^\alpha}{K_\Phi}\left(\alpha^{-\alpha} + \alpha^{-1}\right)\right)^{1/(\alpha-1)} - \frac{\pi}{4}, \tag{A.15}$$

while the amplitude reads

$$\left|\tilde{f}(\omega)\right| = K_A \left(\frac{\omega}{\alpha K_\Phi}\right)^{\beta/(\alpha-1)} \sqrt{2\pi} \underbrace{\left(K_\Phi \alpha(\alpha-1)\left(\frac{\omega}{\alpha K_\Phi}\right)^{(\alpha-2)/(\alpha-1)}\right)^{-1/2}}_{1/\sqrt{\ddot{\Phi}}} \tag{A.16}$$

$$= K_A (\alpha K_\Phi)^{\frac{\beta-1/2}{\alpha-1}} \omega^{\frac{\beta-(\alpha-2)/2}{\alpha-1}} \sqrt{\frac{2\pi}{\alpha-1}}. \tag{A.17}$$

The last complication is the fact that the phase appears in the expression for the waveform (1.75) not with a complex exponential, but instead with a cosine or a sine: this is not a problem, we just need to use the relations $\cos x = (e^{ix} + e^{-ix})/2$ and $\sin x = (e^{ix} - e^{-ix})/2i$. The factor of $i$ in the sine will correspond to a $\pi/2$ phase difference between the two polarizations, while the average of the two different exponentials will correspond to an amplitude reduction of a factor 2 if we restrict ourselves to positive frequencies.[33]

---

[33] Since the Fourier transform is linear the two exponentials can be treated separately. The transform of a real signal is fully encoded by its positive-frequency components; in order for the integral not to vanish in the Gaussian approximation there needs to be a stationary point; the phase of the GW signal is strictly monotonic. These three assumptions lead to the fact that only one of the two exponentials will give a nonzero contribution while the other will have no stationary point, so only the division by 2 will matter in the average.

Substituting the values for $\alpha$, $\beta$, $K_\Phi$ and $K_A$ we get the following expressions [Mag07, eqs. 4.34–37], written in terms of $f = \omega/2\pi$:

$$\widetilde{h}_+(f) = \frac{1}{\pi^{2/3}} \sqrt{\frac{5}{24}} \frac{c}{r} \left(\frac{G\mathcal{M}_c}{c^3}\right)^{5/6} f^{-7/6} \exp\left(\frac{3i}{4}\left(\frac{G\mathcal{M}_c}{c^3} 8\pi f\right)^{-5/3} - i\frac{\pi}{4}\right)\left(\frac{1+\cos^2\iota}{2}\right)$$
(A.18)

$$\widetilde{h}_+(f) = \frac{1}{\pi^{2/3}} \sqrt{\frac{5}{24}} \frac{c}{r} \left(\frac{G\mathcal{M}_c}{c^3}\right)^{5/6} f^{-7/6} \exp\left(\frac{3i}{4}\left(\frac{G\mathcal{M}_c}{c^3} 8\pi f\right)^{-5/3} + i\frac{\pi}{4}\right)\cos\iota.$$
(A.19)

The frequency dependence of the amplitude comes out to be $\left|\widetilde{f}(\omega)\right| \propto \omega^{-7/6} \propto f^{-7/6}$: it might be surprising to see that this is decreasing while the chirping waveform rises in amplitude! The reason for this fact is that each portion of the Fourier integral is weighted not only by the amplitude of the envelope $A(t)$ but also by the time the waveform "spends" in that frequency region, which decreases with time. These two effects compete, but $A \sim \tau^{-1/4}$ while the time spent in the frequency region is measured by $1/\sqrt{\ddot{\Phi}} \sim 1/\sqrt{\tau^{-11/8}} = \tau^{+11/16}$, so the latter wins: $\left|\widetilde{h}(f)\right| \sim \tau^{7/16} \propto \omega^{-7/6}$.

# B   Acronyms

**ADM**  Arnowitt, Deser, Misner

**BBH**  binary black hole

**BH**  black hole

**BNS**  binary neutron star

**CBC**  compact binary coalescence

**EOB**  effective one-body

**EMRI**  Extreme Mass Ratio Inspiral

**FFT**  fast Fourier transform

**IMR**  Inspiral-Merger-Ringdown

**KDE**  Kernel Density Estimate

**LAL**  LIGO Algorithm Library

**LIGO**  laser interferometer gravitational-wave observatory

**GR**  general relativity

**GW**  gravitational wave

**MCMC**  Monte Carlo markov chain

**ML** machine learning

**MH** Metropolis-Hastings

**MOTPE** multi-objective tree-structured Parzen estimator

**NN** neural network

**NR** numerical relativity

**NS** neutron star

**PDF** probability density function

**PN** post-Newtonian

**PCA** principal component analysis

**PSD** power spectral density

**TPE** tree-structured Parzen estimator

`mlgw_bns` machine learning gravitational waves from binary neutron stars

**SGWB** stochastic gravitational wave background

**SNR** signal-to-noise ratio (see section 1.3)

**SPA** stationary phase approximation (see appendix A)

**TT** transverse-traceless

# Contents

# References

[Abb+17]   B. P. Abbott et al. "GW170817: Observation of Gravitational Waves from a
Binary Neutron Star Inspiral".
In: *Physical Review Letters* 119.16 (Oct. 16, 2017), p. 161101.
ISSN: 0031-9007, 1079-7114. DOI: 10.1103/PhysRevLett.119.161101.
URL: https://link.aps.org/doi/10.1103/PhysRevLett.119.161101 (visited
on 2021-04-04) (cit. on pp. 1, 13, 19, 28).

[Aji+11]   P. Ajith et al. *Data Formats for Numerical Relativity Waves*. Feb. 24, 2011.
arXiv: 0709.0093 [gr-qc].
URL: http://arxiv.org/abs/0709.0093 (visited on 2021-03-03) (cit. on p. 16).

[Aki+19]   Takuya Akiba et al.
*Optuna: A Next-Generation Hyperparameter Optimization Framework*.
July 25, 2019. arXiv: 1907.10902 [cs, stat].
URL: http://arxiv.org/abs/1907.10902 (visited on 2021-04-30) (cit. on p. 44).

[BYC13]     J Bergstra, D Yamins, and D D Cox.
            "Making a Science of Model Search: Hyperparameter Optimization in
            Hundreds of Dimensions for Vision Architectures". In: (2013), p. 9
            (cit. on p. 46).

[Ber+11]    James Bergstra et al. "Algorithms for Hyper-Parameter Optimization".
            In: *Advances in Neural Information Processing Systems*. Vol. 24.
            Curran Associates, Inc., 2011. URL: https:
            //papers.nips.cc/paper/2011/hash/86e8f7ab32cfd12577bc2619bc635690-
            Abstract.html (visited on 2021-08-15) (cit. on p. 44).

[BB21]      Sebastiano Bernuzzi and Matteo Breschi. *Notes on Gravitational Waves*. 2021.
            URL: http://sbernuzzi.gitpages.tpi.uni-jena.de/gw/ (cit. on p. 34).

[BDG20]     Donato Bini, Thibault Damour, and Andrea Geralico.
            "Binary Dynamics at the Fifth and Fifth-and-a-Half Post-Newtonian Orders".
            In: (Mar. 26, 2020). DOI: 10.1103/PhysRevD.102.024062.
            URL: https://arxiv.org/abs/2003.11891v1 (visited on 2021-07-21)
            (cit. on p. 32).

[Bla14]     Luc Blanchet. "Gravitational Radiation from Post-Newtonian Sources and
            Inspiralling Compact Binaries".
            In: *Living Reviews in Relativity* 17.1 (Dec. 2014), p. 2. ISSN: 2367-3613, 1433-8351.
            DOI: 10.12942/lrr-2014-2. URL:
            http://link.springer.com/10.12942/lrr-2014-2 (visited on 2021-04-04)
            (cit. on p. 31).

[BGB21]     Matteo Breschi, Rossella Gamba, and Sebastiano Bernuzzi.
            *${\tt Bajes}$: Bayesian Inference of Multimessenger Astrophysical Data, Methods
            and Application to Gravitational-Waves*. Jan. 29, 2021.
            arXiv: 2102.00017 [astro-ph, physics:gr-qc].
            URL: http://arxiv.org/abs/2102.00017 (visited on 2021-05-03)
            (cit. on pp. 17, 46).

[Car19]     Sean M. Carroll. *Spacetime and Geometry: An Introduction to General Relativity*.
            New York: Cambridge University Press, 2019. 1 p. ISBN: 978-1-108-77038-5
            (cit. on pp. 7, 8).

[CF98]      E. Chassande-Mottin and P. Flandrin.
            "On the Stationary Phase Approximation of Chirp Spectra".
            In: *Proceedings of the IEEE-SP International Symposium on Time-Frequency and
            Time-Scale Analysis (Cat. No.98TH8380)*.
            International Symposium on Time-Frequency and Time-Scale Analysis.
            Pittsburgh, PA, USA: IEEE, 1998, pp. 117–120. ISBN: 978-0-7803-5073-1.
            DOI: 10.1109/TFSA.1998.721375.
            URL: http://ieeexplore.ieee.org/document/721375/ (visited on 2021-08-24)
            (cit. on p. 50).

[Col18]    LIGO Scientific Collaboration. *LIGO Algorithm Library*.
           LIGO Scientific Collaboration, 2018. DOI: 10.7935/GT1W-FZ16.
           URL: https://git.ligo.org/lscsoft/lalsuite (visited on 2021-08-27)
           (cit. on p. 33).

[Dam14]    Thibault Damour.
           *The General Relativistic Two Body Problem and the Effective One Body Formalism*.
           2014. DOI: 10.1007/978-3-319-06349-2_5.
           arXiv: 1212.3169 [gr-qc, physics:hep-th].
           URL: http://arxiv.org/abs/1212.3169 (visited on 2021-08-28) (cit. on p. 33).

[Ein16]    Albert Einstein.
           "Näherungsweise Integration Der Feldgleichungen Der Gravitation".
           In: *Sitzungsberichte der Königlich Preußischen Akademie der Wissenschaften (Berlin*
           (Jan. 1, 1916), pp. 688–696.
           URL: https://ui.adsabs.harvard.edu/abs/1916SPAW.......688E (visited on
           2021-08-17) (cit. on p. 4).

[Fav11]    Marc Favata. "The Gravitational-Wave Memory from Eccentric Binaries".
           In: *Physical Review D* 84.12 (Dec. 6, 2011), p. 124013. ISSN: 1550-7998, 1550-2368.
           DOI: 10.1103/PhysRevD.84.124013. arXiv: 1108.3121.
           URL: http://arxiv.org/abs/1108.3121 (visited on 2021-08-22) (cit. on p. 22).

[Fav+21]   Marc Favata et al. *Constraining the Orbital Eccentricity of Inspiralling Compact
           Binary Systems with Advanced LIGO*. Aug. 12, 2021. arXiv: 2108.05861 [gr-qc].
           URL: http://arxiv.org/abs/2108.05861 (visited on 2021-08-22) (cit. on p. 22).

[Fin92]    Lee Samuel Finn. *Detection, Measurement and Gravitational Radiation*.
           Sept. 24, 1992. DOI: 10.1103/PhysRevD.46.5236. arXiv: gr-qc/9209010.
           URL: http://arxiv.org/abs/gr-qc/9209010 (visited on 2021-08-23)
           (cit. on p. 25).

[FH08]     Eanna E. Flanagan and Tanja Hinderer. "Constraining Neutron Star Tidal Love
           Numbers with Gravitational Wave Detectors".
           In: *Physical Review D* 77.2 (Jan. 22, 2008), p. 021502. ISSN: 1550-7998, 1550-2368.
           DOI: 10.1103/PhysRevD.77.021502. arXiv: 0709.1915.
           URL: http://arxiv.org/abs/0709.1915 (visited on 2020-11-13) (cit. on p. 20).

[GS16]     Chad R. Galley and Patricia Schmidt. *Fast and Efficient Evaluation of
           Gravitational Waveforms via Reduced-Order Spline Interpolation*. Nov. 22, 2016.
           arXiv: 1611.07529 [gr-qc].
           URL: http://arxiv.org/abs/1611.07529 (visited on 2021-08-28) (cit. on p. 49).

[GBN20]    Rossella Gamba, Sebastiano Bernuzzi, and Alessandro Nagar. *Fast, Faithful,
           Frequency-Domain Effective-One-Body Waveforms for Compact Binary Coalescences*.
           Nov. 30, 2020. arXiv: 2012.00027 [astro-ph, physics:gr-qc].
           URL: http://arxiv.org/abs/2012.00027 (visited on 2021-02-27) (cit. on p. 34).

[Gou07]     Eric Gourgoulhon. *3+1 Formalism and Bases of Numerical Relativity*. Mar. 6, 2007.
            arXiv: gr-qc/0703035.
            URL: http://arxiv.org/abs/gr-qc/0703035 (visited on 2021-04-13)
            (cit. on p. 32).

[Har+20]    Charles R. Harris et al. "Array Programming with NumPy".
            In: *Nature* 585.7825 (7825 Sept. 2020), pp. 357–362. ISSN: 1476-4687.
            DOI: 10.1038/s41586-020-2649-2.
            URL: https://www.nature.com/articles/s41586-020-2649-2 (visited on
            2021-09-07) (cit. on p. 47).

[HT75]      R. A. Hulse and J. H. Taylor. "Discovery of a Pulsar in a Binary System".
            In: *The Astrophysical Journal Letters* 195 (Jan. 1, 1975), pp. L51–L53.
            ISSN: 0004-637X. DOI: 10.1086/181708.
            URL: http://adsabs.harvard.edu/abs/1975ApJ...195L..51H (visited on
            2020-07-13) (cit. on p. 21).

[Ken07]     Daniel Kennefick. *Traveling at the Speed of Thought*. 2007.
            ISBN: 978-0-691-11727-0. URL: https:
            //press.princeton.edu/books/hardcover/9780691117270/traveling-at-
            the-speed-of-thought (visited on 2021-08-17) (cit. on p. 4).

[KB17]      Diederik P. Kingma and Jimmy Ba. *Adam: A Method for Stochastic Optimization*.
            Jan. 29, 2017. arXiv: 1412.6980 [cs].
            URL: http://arxiv.org/abs/1412.6980 (visited on 2021-08-15) (cit. on p. 44).

[Kum+15]    Prayush Kumar et al. "Accuracy and Precision of Gravitational-Wave Models
            of Inspiraling Neutron Star – Black Hole Binaries with Spin: Comparison with
            Numerical Relativity in the Low-Frequency Regime".
            In: *Physical Review D* 92.10 (Nov. 4, 2015), p. 102001. ISSN: 1550-7998, 1550-2368.
            DOI: 10.1103/PhysRevD.92.102001. arXiv: 1507.00103.
            URL: http://arxiv.org/abs/1507.00103 (visited on 2021-03-31) (cit. on p. 33).

[Lac+17]    Benjamin D. Lackey et al. "Effective-One-Body Waveforms for Binary Neutron
            Stars Using Surrogate Models".
            In: *Physical Review D* 95.10 (May 30, 2017), p. 104036.
            ISSN: 2470-0010, 2470-0029. DOI: 10.1103/PhysRevD.95.104036.
            arXiv: 1610.04742.
            URL: http://arxiv.org/abs/1610.04742 (visited on 2020-11-20) (cit. on p. 1).

[Lac+19]    Benjamin D. Lackey et al.
            "Surrogate Model for an Aligned-Spin Effective One Body Waveform Model
            of Binary Neutron Star Inspirals Using Gaussian Process Regression".
            In: *Physical Review D* 100.2 (July 3, 2019), p. 024002. ISSN: 2470-0010, 2470-0029.
            DOI: 10.1103/PhysRevD.100.024002. arXiv: 1812.08643.
            URL: http://arxiv.org/abs/1812.08643 (visited on 2021-02-26) (cit. on p. 50).

[LP07]     James M. Lattimer and Maddapa Prakash.
           "Neutron Star Observations: Prognosis for Equation of State Constraints".
           In: *Physics Reports* 442.1-6 (Apr. 2007), pp. 109–165. ISSN: 03701573.
           DOI: 10.1016/j.physrep.2007.02.003. arXiv: astro-ph/0612440.
           URL: http://arxiv.org/abs/astro-ph/0612440 (visited on 2020-09-26)
           (cit. on p. 20).

[LC21]     Alexandre Le Tiec and Marc Casals. "Spinning Black Holes Fall in Love".
           In: *Physical Review Letters* 126.13 (Mar. 30, 2021), p. 131102.
           DOI: 10.1103/PhysRevLett.126.131102.
           URL: https://link.aps.org/doi/10.1103/PhysRevLett.126.131102 (visited
           on 2021-08-21) (cit. on p. 20).

[LIG+16]   LIGO Scientific Collaboration and Virgo Collaboration et al.
           "Observation of Gravitational Waves from a Binary Black Hole Merger".
           In: *Physical Review Letters* 116.6 (Feb. 11, 2016), p. 061102.
           DOI: 10.1103/PhysRevLett.116.061102.
           URL: https://link.aps.org/doi/10.1103/PhysRevLett.116.061102 (visited
           on 2020-03-23) (cit. on p. 13).

[Lin84]    L. Lindblom. "Limits on the Gravitational Redshift Form Neutron Stars".
           In: *The Astrophysical Journal* 278 (Mar. 1, 1984), pp. 364–368. ISSN: 0004-637X.
           DOI: 10.1086/161800.
           URL: https://ui.adsabs.harvard.edu/abs/1984ApJ...278..364L (visited on
           2021-08-20) (cit. on p. 20).

[LL11]     Ka-Wai Lo and Lap-Ming Lin.
           "THE SPIN PARAMETER OF UNIFORMLY ROTATING COMPACT STARS".
           In: *The Astrophysical Journal* 728.1 (Jan. 2011), p. 12. ISSN: 0004-637X.
           DOI: 10.1088/0004-637X/728/1/12.
           URL: https://doi.org/10.1088/0004-637x/728/1/12 (visited on 2021-08-20)
           (cit. on p. 18).

[Löf+12]   Frank Löffler et al. "The Einstein Toolkit: A Community Computational
           Infrastructure for Relativistic Astrophysics".
           In: *Classical and Quantum Gravity* 29.11 (June 7, 2012), p. 115001.
           ISSN: 0264-9381, 1361-6382. DOI: 10.1088/0264-9381/29/11/115001.
           arXiv: 1111.3344.
           URL: http://arxiv.org/abs/1111.3344 (visited on 2021-08-27) (cit. on p. 33).

[Mag07]    Michele Maggiore. *Gravitational Waves: Volume 1: Theory and Experiments*.
           1 edition. Oxford: Oxford University Press, Nov. 24, 2007. 576 pp.
           ISBN: 978-0-19-857074-5
           (cit. on pp. 5, 9, 10, 12–14, 16, 17, 21–23, 25, 31, 32, 35, 55).

[Mag18]    Michele Maggiore. *Gravitational Waves: Volume 2: Astrophysics and Cosmology*.
           Oxford: Oxford University Press, May 22, 2018. 848 pp.
           ISBN: 978-0-19-857089-9 (cit. on pp. 19, 20).

[MN17]     Bryan F. J. Manly and Jorge A. Navarro Alberto.
           *Multivariate Statistical Methods: A Primer*. Fourth edition.
           Boca Raton: CRC Press, Taylor & Francis Group, 2017. 253 pp.
           ISBN: 978-1-4987-2896-6 (cit. on p. 38).

[MCB15]    Christopher J. Moore, Robert H. Cole, and Christopher P. L. Berry.
           "Gravitational-Wave Sensitivity Curves".
           In: *Classical and Quantum Gravity* 32.1 (Jan. 8, 2015), p. 015014.
           ISSN: 0264-9381, 1361-6382. DOI: 10.1088/0264-9381/32/1/015014.
           arXiv: 1408.0740.
           URL: http://arxiv.org/abs/1408.0740 (visited on 2020-04-19) (cit. on p. 26).

[NBR21]    Alessandro Nagar, Alice Bonino, and Piero Rettegno.
           *All in One: Effective One Body Multipolar Waveform Model for Spin-Aligned,*
           *Quasi-Circular, Eccentric, Hyperbolic Black Hole Binaries*. Jan. 26, 2021.
           arXiv: 2101.08624 [gr-qc].
           URL: http://arxiv.org/abs/2101.08624 (visited on 2021-02-26) (cit. on p. 34).

[Nag+18]   Alessandro Nagar et al.
           *Time-Domain Effective-One-Body Gravitational Waveforms for Coalescing Compact*
           *Binaries with Nonprecessing Spins, Tides and Self-Spin Effects*. Oct. 28, 2018.
           DOI: 10.1103/PhysRevD.98.104052. arXiv: 1806.01772 [gr-qc].
           URL: http://arxiv.org/abs/1806.01772 (visited on 2021-02-27)
           (cit. on pp. 2, 34).

[Ned+20]   Vsevolod Nedora et al.
           *Numerical Relativity Simulations of the Neutron Star Merger GW170817: Long-Term*
           *Remnant Evolutions, Winds, Remnant Disks, and Nucleosynthesis*. Aug. 12, 2020.
           arXiv: 2008.04333 [astro-ph, physics:gr-qc].
           URL: http://arxiv.org/abs/2008.04333 (visited on 2020-11-16) (cit. on p. 33).

[Nie15]    Michael A. Nielsen. *Neural Networks and Deep Learning*.
           Determination Press, 2015.
           URL: http://neuralnetworksanddeeplearning.com (visited on 2021-03-23)
           (cit. on pp. 41, 43).

[Oza+20]   Yoshihiko Ozaki et al. "Multiobjective Tree-Structured Parzen Estimator for
           Computationally Expensive Optimization Problems".
           In: *Proceedings of the 2020 Genetic and Evolutionary Computation Conference*.
           GECCO '20.
           New York, NY, USA: Association for Computing Machinery, June 25, 2020,
           pp. 533–541. ISBN: 978-1-4503-7128-5. DOI: 10.1145/3377930.3389817.
           URL: https://doi.org/10.1145/3377930.3389817 (visited on 2021-08-15)
           (cit. on p. 44).

[Pea01]    Karl Pearson.
           "LIII. On Lines and Planes of Closest Fit to Systems of Points in Space".
           In: *The London, Edinburgh, and Dublin Philosophical Magazine and Journal of*
           *Science* 2.11 (Nov. 1, 1901), pp. 559–572. ISSN: 1941-5982.

DOI: 10.1080/14786440109462720.
URL: https://doi.org/10.1080/14786440109462720 (visited on 2021-08-13)
(cit. on p. 38).

[Ped+11]    Fabian Pedregosa et al. "Scikit-Learn: Machine Learning in Python".
In: *Journal of Machine Learning Research* 12.85 (2011), pp. 2825–2830. URL:
http://jmlr.org/papers/v12/pedregosa11a.html (visited on 2021-08-14)
(cit. on pp. 42, 44).

[Rud16]    Sebastian Ruder.
"An Overview of Gradient Descent Optimization Algorithms".
In: (Sept. 15, 2016).
URL: https://arxiv.org/abs/1609.04747v2 (visited on 2021-08-15)
(cit. on p. 44).

[Sch+20]    Stefano Schmidt et al.
*Machine Learning Gravitational Waves from Binary Black Hole Mergers*.
Nov. 3, 2020. arXiv: 2011.01958 [gr-qc].
URL: http://arxiv.org/abs/2011.01958 (visited on 2020-11-13)
(cit. on pp. 2, 41).

[TW82]    J. H. Taylor and J. M. Weisberg. "A New Test of General Relativity -
Gravitational Radiation and the Binary Pulsar PSR 1913+16".
In: *The Astrophysical Journal* 253 (Feb. 1, 1982), pp. 908–920. ISSN: 0004-637X.
DOI: 10.1086/159690.
URL: http://adsabs.harvard.edu/abs/1982ApJ...253..908T (visited on
2020-07-13) (cit. on p. 21).

[Tea11]    ET Science Team. *Einstein Gravitational Wave Telescope Conceptual Design Study*.
2011. URL: http://www.et-gw.eu (cit. on p. 23).

[Wal09]    Robert M. Wald. *Introduction to Gravitational Self-Force*. July 2, 2009.
arXiv: 0907.0412 [gr-qc].
URL: http://arxiv.org/abs/0907.0412 (visited on 2021-06-09) (cit. on p. 29).